3-22-2019

Modeling High-Altitude Nuclear Detonations using Existing Ionospheric Models

Sophia G. Schwalbe

Recommended Citation

Schwalbe, Sophia G., "Modeling High-Altitude Nuclear Detonations using Existing Ionospheric Models" (2019). *Theses and Dissertations*. 2208.
https://scholar.afit.edu/etd/2208

Modeling High-Altitude Nuclear Detonations
Using Existing Ionospheric Models

THESIS

Sophia G. Schwalbe, 2d Lt, USAF

AFIT-ENP-MS-19-M-092

DEPARTMENT OF THE AIR FORCE
AIR UNIVERSITY

AIR FORCE INSTITUTE OF TECHNOLOGY

Wright-Patterson Air Force Base, Ohio

AFIT-ENP-MS-19-M-092

MODELING HIGH-ALTITUDE NUCLEAR DETONATIONS USING EXISTING IONOSPHERIC MODELS

THESIS

Presented to the Faculty
Department of Engineering Physics
Graduate School of Engineering and Management
Air Force Institute of Technology
Air University
Air Education and Training Command
in Partial Fulfillment of the Requirements for the
Degree of Master of Science in Applied Physics

Sophia G. Schwalbe, B.S.
2d Lt, USAF

March 2019

DISTRIBUTION STATEMENT A
APPROVED FOR PUBLIC RELEASE; DISTRIBUTION UNLIMITED.

AFIT-ENP-MS-19-M-092

MODELING HIGH-ALTITUDE NUCLEAR DETONATIONS USING EXISTING IONOSPHERIC MODELS

THESIS

Sophia G. Schwalbe, B.S.
2d Lt, USAF

Committee Membership:

Robert D. Loper, Ph.D.
Chair

Maj Charlton D. Lewis, Ph.D.
Member

Maj Omar Nava, Ph.D.
Member

AFIT-ENP-MS-19-M-092

Abstract

One threat to the United States is a nuclear weapon being detonated at high altitude over the country. The resulting electromagnetic pulse (EMP) could devastate the nation. Despite its destructive nature, the response of the ionosphere to such an event is poorly understood. This study assesses if existing ionospheric models, which are used to nowcast and forecast ionospheric changes, can be used to model the response to a high-altitude nuclear detonation (HAND). After comparing five ionosphere models, the Thermosphere-Ionosphere-Electrodynamics General Circulation Model (TIE-GCM) was selected and modified to incorporate an array of F10.7 indices to serve as a proxy for the localized heightened extreme ultraviolet activity and, using the temperature of the fireball attenuated over distance, drive the chemistry. It was found that the modified model had an increase in electron content over the standard model that was in good agreement with the changes resulting from a geomagnetic storm. However, the examined ionospheric models are not sufficient to simulate the effects of a HAND due to the limitations in the models' calculations.

Acknowledgements

I would like to begin by thanking all those that have helped me while at AFIT. First, I would like to thank my advisor, Dr. Loper, for letting me have creative reign on this study while still remaining supportive. I must also thank Maj Lewis for strongly encouraging me to choose this as my topic. I did not know it then, but I found a true passion in the subject area. I would also like to acknowledge the support and advice from Maj Nava and the many discussions we had. It would also be remiss of me not to recognize the help provided by Dr. Sean Elvidge of the University of Birmingham, whose assistance made it possible for me to actually run the model. And lastly, I would like to thank my parents, who both greatly assisted me with edits and with moral support throughout the entire process.

This research was developed with funding from the Defense Advanced Research Projects Agency, Defense Science Office (DARPA/DSO). The views, opinions, and/or findings expressed are those of the author and should not be interpreted as representing the official views or policies of the Department of Defense or the U.S. Government.

This publication makes use of data from the Qaanaaq ionosonde, owned by the U.S. Air Force Research Laboratory Space Vehicles Directorate and supported in part by the Air Force Office of Scientific Research. The author thanks Svend Erik Ascanius of the Danish Meteorological Institute for its operation.

The USU-GAIM Model was developed by the GAIM team (R.W. Schunk, L. Scherliess, J.J. Sojka, D.C. Thompson, L. Zhu) at Utah State University.

Sophia G. Schwalbe

Table of Contents

Page

List of Figures

List of Tables

List of Acronyms

ARPA Advanced Research Projects Agency

ASTM American Society for Testing and Materials

CCMC Community Coordinated Modeling Center

DARPA Defense Advanced Research Projects Agency

DIDBase Digital Ionogram DataBase

DoD Department of Defense

DOE Department of Energy

DTRA Defense Threat Reduction Agency

EMP Electromagnetic Pulse

ESA European Space Agency

EUV Extreme Ultraviolet

EUVAC EUV Flux Model for Aeronomic Calculations

F10.7 Solar radio flux at 10.7 cm

foE Peak Frequency of the *E*-region

GIRO Global Ionospheric Radio Observatory

GITM Global Ionosphere Thermosphere Model

GNSS Global Navigation Satellite System

GPS Global Positioning System

HAND High-Altitude Nuclear Detonation

HAO High Altitude Observatory

HEMP High-Altitude Electromagnetic Pulse

hmE Peak Altitude of the E-region

hmF2 Peak Altitude of the F_2-region

HPI Hemispheric Power Index

HWM Horizontal Wind Model

ICBM Intercontinental Ballistic Missile

IFM Interplanetary Magnetic Field

IGRF International Geomagnetic Reference Field

MHD Magnetohydrodynamics

N$_e$ Electron Number Density

NASA National Aeronautics and Space Administration

NCAR National Center for Atmospheric Research

nmE Peak Electron Density of the E-region

nmF2 Peak Electron Density of the F_2-region

OCR Omnidirectional Counting Rates

SAMI3 Sami3 is Also a Model of the Ionosphere

sfu Solar Flux Units, $[\times 10^{-22}\ \mathrm{W\ Hz^{-1} m^{-2}}]$

TEC	Total Electron Content
TECU	Total Electron Content Units, [$\times 10^{16} \mathrm{m}^{-2}$]
TIE-GCM	Thermosphere-Ionosphere-Electrodynamics General Circulation Model
USAF	United States Air Force
USU-GAIM	Utah State University - Global Assimilation of Ionospheric Measurements
UTC	Coordinated Universal Time

I. Introduction

1.1 Motivation

In October 1957, the U.S.S.R. launched the Sputnik 1 satellite into low Earth orbit using an R-7 rocket. Concerned that the U.S.S.R. now had the capability to launch nuclear weapons, the U.S. began investigating ways to intercept and destroy these missiles. At the Lawrence Radiation Laboratory, now Lawrence Livermore National Laboratory, Greek physicist Nicholas Christofilos proposed the detonation of a nuclear bomb at high altitude, which would result in electrons being trapped by Earth's magnetic field and destroying any missile passing through them (Gombosi et al., 2017). This was termed the Christofilos Effect. A series of nuclear tests began, first conducted by the U.S. and later by the U.S.S.R., which took place at altitudes greater than 20 km. The Advanced Research Projects Agency (ARPA) conducted the first tests specifically for high altitude nuclear detonations (HANDs) in 1958, known as the Argus experiments. The Argus experiments had three test detonations, all with a yield of 1.7 kT and detonated at heights around 300 miles, or 483 km. These tests demonstrated the effect that Christofilos had proposed and proved that the generated electrons could also damage low orbit satellites. In total, the U.S. conducted 11 high altitude tests, while the U.S.S.R. reportedly conducted seven, reported in Table 1. These tests were halted in 1963 after the signing of the Limited Nuclear Test Ban Treaty.

Table 1. List of the reported HAND tests in the period between 1958 and 1962, with altitude, yield, date, and the country that conducted the tests (Gombosi et al., 2017), verified using material from U.S. Department of Energy (2015).

Operation	Test	Country	Date	Altitude [km]	Yield [kT]
HARDTACK I	Yucca	U.S.A.	28 Apr 1958	26	1.7
HARDTACK I	Teak	U.S.A.	1 Aug 1958	77	3800
HARDTACK I	Orange	U.S.A.	12 Aug 1958	43	3800
ARGUS	Argus I	U.S.A.	27 Aug 1958	∼483	1.7
ARGUS	Argus II	U.S.A.	30 Aug 1958	∼483	1.7
ARGUS	Argus III	U.S.A.	6 Sep 1958	∼483	1.7
-	Test #88	U.S.S.R.	6 Sep 1961	23	10.5
-	Test #115	U.S.S.R.	6 Oct 1961	41	40
K PROJECT	Test #127	U.S.S.R.	27 Oct 1961	150	1.2
K PROJECT	Test #128	U.S.S.R.	27 Oct 1961	300	1.2
FISHBOWL	Starfish	U.S.A.	9 July 1962	400	1400
FISHBOWL	Checkmate	U.S.A.	20 Oct 1962	Tens of km	Low
K PROJECT	Test #184	U.S.S.R.	22 Oct 1962	290	300
FISHBOWL	Bluegill	U.S.A.	26 Oct 1962	Tens of km	<1,000
K PROJECT	Test #187	U.S.S.R.	28 Oct 1962	150	300
FISHBOWL	Kingfish	U.S.A.	1 Nov 1962	Tens of km	<1,000
K PROJECT	Test #195	U.S.S.R.	1 Nov 1962	59	300
FISHBOWL	Tightrope	U.S.A.	4 Nov 1962	Tens of km	Low

The most famous of the high altitude nuclear detonations was Starfish Prime, a 1.4 MT weapon carried on a Thor missile detonated at an altitude of 400 km over Johnston Island in the Pacific Ocean on 9 July 1962. This test was the first time the effects of an electromagnetic pulse (EMP) were observed. In Hawaii, 1,300 km away from the detonation, streetlights were extinguished, local radio stations were shut down, telephone communications were cut off, and burglar alarms were triggered (Dupont, 2004). It was also the test with the most collected data: one day after the detonation, the Telstar-1 satellite was launched with the most advanced on-board sensors at the time. This satellite was the result of a collaboration between AT&T; Bell Labs; NASA; the British General Post Office; and the French National Post, Telegraph, and Telecom Office. Its primary mission was communications. However, because of the NASA collaboration, Telstar-1 was also outfitted with a number of sensors used to measure radiation damage to its solar cells and transistors as well as proton and electron radiation. Given that it was launched one day after the Starfish Prime test, the Telstar-1 satellite received a high dose of radiation that eventually resulted in its failure in February of the following year. Fortunately, it gathered an unprecedented amount of data on the effects of a HAND and on the structure of the Van Allen radiation belts.

The series of HANDs demonstrated the effectiveness of nuclear weapons in space. In fact, Telstar-1 was not the only satellite to fail due to the effects of the nuclear tests. At least six satellites were determined to have failed from radiation effects, and several more were damaged, described in Table 2. The full extent of the damage caused by Starfish Prime alone is unknown, since many satellites in orbit at the time were either classified military assets or they did not have sufficient diagnostic tools on-board to determine if damage was received.

Table 2. A list of reported damage to satellites from the Starfish Prime test on 9 July 1962. The list was initially composed of six satellites in a 1963 report, but was expanded in 2010. It is thought that many more satellites were damaged, but due to the nature of the satellites in orbit or the lack of reporting and diagnostics, these satellites were not included. The list was compiled from Gombosi et al. (2017) and Conrad et al. (2010).

Satellite	Date Launched	Date Terminated	Damage
Transit-4B	15 Nov 1961	2 Aug 1962	Solar panel output decrease, solar cell damage and failure
TRAAC	15 Nov 1961	12 Aug 1962	Solar cell damage, transmission stopped 36 days after Starfish Prime
OSO-1	7 Mar 1962	6 Aug 1963	Solar array degradation, power cell failure
Ariel-1	26 Apr 1962	Nov 1964	Solar cell degradation, loss of modulation on real-time telemetry and tape recorders
Kosmos-5	28 May 1962	2 May 1963	Radiation damage
Telstar-1	10 Jul 1962	21 Feb 1963	Failure of command decoder, failure of command system, ionization damage to transistors
Alouette-1	29 Sep 1962	30 Sep 1972	Battery degradation
Explorer 14	2 Oct 1962	8 Oct 1963	Encoder malfunction, solar cell damage
Explorer 15	27 Oct 1962	9 Feb 1963	Encoder failure, failure from under-voltage
Anna-1B	31 Oct 1962	-	Solar cell deterioration

Due to the devastating effects of historical HANDs on the fledgling satellite network in the early 1960s and the observed effects of the EMP from Starfish Prime on

Honolulu, many countries incorporate EMPs into their military doctrine. This has become increasingly important in modern warfare, primarily due to the reliance on GPS (Global Positioning System), radio, and cellular communication networks. In 2001, the U.S. established the EMP Commission in order to assess EMP threats from foreign adversaries and the U.S.'s EMP vulnerability. Currently, Russia, Iran, China, and North Korea all include EMPs as viable measures of attack in their strategic plans. North Korea, as recently as early 2018, threatened to detonate a nuclear device at high altitude over the Pacific Ocean with the intent to cripple Guam and the military installations there.

In an effort to characterize a HAND, multiple U.S. agencies began studying HANDs and their effects. Specifically, many agencies are developing models that can predict the effects of a HAND, including EMPs and ionospheric effects. Software exists to model an EMP, but few simulations include the atmospheric effects that can influence the behavior of the emitted radiation as most models assume a quiet atmosphere and ionosphere with no anomalies caused by solar flares or geomagnetic storms. It is well known that such natural phenomena can significantly influence the total electron content (TEC), the vertical structure of the ionosphere, the creation of artificial Van Allen radiation belts, and the mechanisms responsible for the decay of the injected high-energy electrons. Conversely, several physics-based ionospheric models exist, but no single model incorporates all ionospheric physics. Furthermore, none are designed to simulate high fluxes of electrons that would occur from a coronal mass ejection or HAND. Thus, there is a gap in the capability in current software models to represent a pulse-like phenomena such as a HAND realistically.

1.2 Research Objective

Due to the complexity of designing a global ionospheric model, it is preferable to modify an existing model of the ionosphere in order to account for nuclear effects, instead of using an EMP or HAND code and changing it to account for ionospheric variations. This research is centered on examining the existing ionospheric models, evaluating their strengths and weaknesses, and determining if any are capable of simulating the effects of a HAND on the ionosphere. This will require modifying the models to include the radiation emitted from a HAND and the resulting effects. The ionosphere model should then be able to produce results that can be compared with data gathered during the high-altitude tests from 1958 to 1962. Even though most of the data from the tests was collected above the ionosphere, the model should be able to recreate the lowest altitude data. Further, the model should be consistent with data collected from radio arrays and satellite sensor data.

This research will first examine the simplest model of the ionosphere, the Chapman model. Then, a set of ionospheric models will be examined, including NeQuick, the Utah State University - Global Assimilation of Ionospheric Measurements model (USU-GAIM), the Global Ionosphere Thermosphere Model (GITM), Sami3 is Also a Model of the Ionosphere (SAMI3), and the Thermosphere-Ionosphere-Electrodynamics General Circulation Model (TIE-GCM). These models were selected due to their availability from NASA's Community Coordinated Modeling Center (CCMC) or from online source codes. First, the various models will be examined to determine if they can be used to simulate HAND effects. Then, the models with available source codes will be modified to demonstrate if the framework and the physics are robust enough to predict such effects. The results of the modified models will then be compared to HAND observations and the "best" model performance will be highlighted. These results will be used to inform future development for a full-physics, magnetohydrodynamics (MHD) coupled, wave/particle ionospheric model for operational use which would be able to compute anomalies such as a HAND by illustrating the shortcomings of the current models.

1.3 Preview

Chapter II provides relevant background information, to include the necessary concepts in nuclear and ionospheric physics and an introduction to the models used in this study. Chapter III describes the methodology applied to analyze the performance of the ionospheric models and to modify the available models. Chapter IV details data analysis and the results of the modified models, and lastly, Chapter V discusses the conclusions and recommendations for future work.

II. Background

To understand the full extent of the physics involved in the problem of a nuclear detonation at high altitude, it is necessary to first discuss what is known about nuclear detonations and their observed effects in the atmosphere, as well as thoroughly examining the physics of the atmosphere where the nuclear device is detonated. For HANDs, this region of the atmosphere includes the ionosphere and the Van Allen radiation belts. Then some detail should be provided about a few of the models that exist for the ionosphere to understand their various strengths and weaknesses before they are investigated for use in modeling a HAND response.

2.1 Nuclear Physics

If modifying an ionospheric model to accommodate a HAND, the physics behind the explosion must be understood. The resulting nuclear products all produce significant effects on the atmosphere and will propagate differently from naturally-occurring electrons or radiation. Most significantly, the fission fragments, gamma rays, and x-rays will be of critical importance and will be examined in detail. Blast and thermal effects typically associated with nuclear weapons will only be mentioned, since at high altitude, these effects are negligible.

2.1.1 Nuclear Weapon Physics

A typical nuclear detonation for a weapon is the result of an induced fission of a heavy, unstable nucleus into two, occasionally three, fission fragments, and free neutrons. For example, uranium, a common nuclear fuel, is bombarded by neutrons to create an unstable compound nucleus which then fissions. This process is often depicted using the liquid drop model (Krane, 1988). The resulting fission fragments are not deterministic; rather, they are the result of a statistical process and follow the well-known double-hump curve as shown in Figure 1.

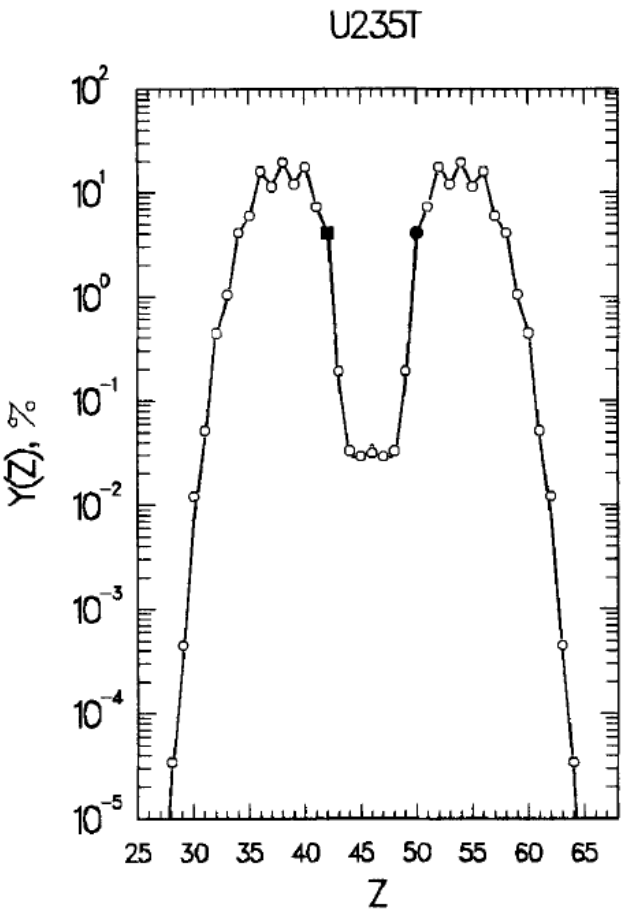

Figure 1. The characteristic double-hump curve of the fission of uranium-235 into its potential fission fragments. The process is statistical in nature, and the probability of the resulting products is given on the vertical axis. This is reproduced from Wahl (1988).

Typically, these fission fragments are radioactive themselves and will follow their decay chains until they reach a stable configuration, using alpha, beta plus, and beta minus decay. Alpha decay involves the parent nucleus losing an alpha particle, or helium nucleus, consisting of two protons and two neutrons, and emits discrete energies unless accompanied by gamma radiation (Krane, 1988).

$$ {}^{A}_{Z}X \rightarrow^{A-4}_{Z-2} X' + \alpha \tag{1} $$

Beta plus decay is the decay of a proton into a neutron, positron, and electron neutrino and is much rarer compared to beta minus decay, where the neutron decays into a proton, electron, and an electron antineutrino. In both beta decays, the energy spectrum is continuous, as the energy of the electron neutrino/antineutrino is continuous as well (Krane, 1988).

$$ {}^{A}_{Z}x \rightarrow^{A}_{Z-1} X' + e^{+} + \nu_e \tag{2} $$

$$ {}^{A}_{Z}X \rightarrow^{A}_{Z+1} X' + e^{-} + \bar{\nu}_e \tag{3} $$

One fission results in the generation of approximately 200 MeV in products. Roughly 85% of the energy is released in the form of fission fragments. Approximately 93% of the prompt energy from the fission reaction, meanwhile, goes to the kinetic energy of the fission fragments, with the remaining fraction being split between neutrons and gamma rays (Bridgman, 2001). Gamma rays will typically only be 0.1-0.3% of the total yield. The kinetic energy of the fission fragments is transformed into radiation that corresponds with x-rays, so anywhere from 70 to 80% of the total yield of a weapon will be in the form of x-rays (Conrad et al., 2010). The remaining yield is split between thermal and blast effects, as shown in Figure 2, though the percentage of x-rays goes up with altitude as the other effects cannot manifest due to decreased environmental interaction.

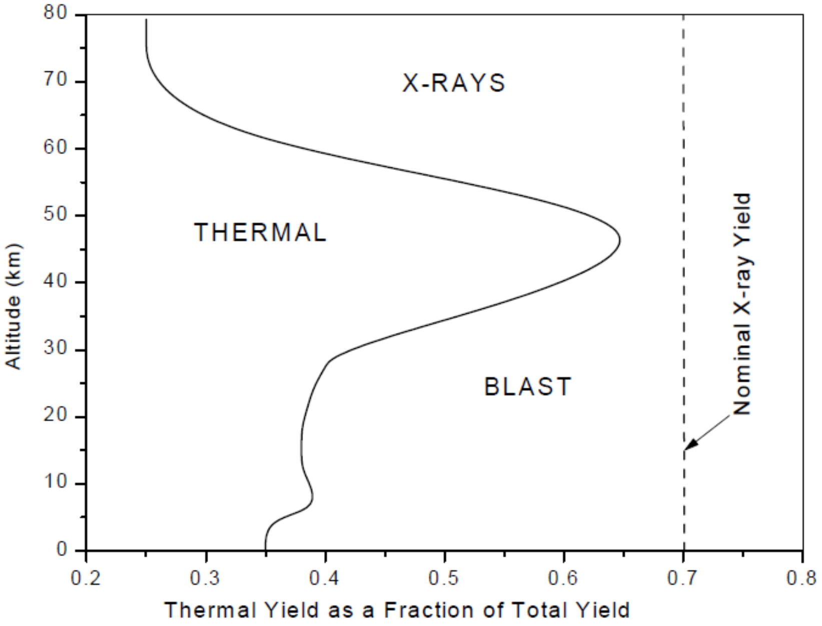

Figure 2. The nominal x-ray yield of a typical nuclear weapon is between 70-80 % of the total yield, shown by the dashed vertical line, with the remaining fraction being split between blast and thermal effects, denoted by the solid line. The exact percentages are highly dependent on the altitude of detonation, with the x-ray yield increasing as the atmosphere thins. Figure taken from Bridgman (2001).

The emitted x-rays from the weapon are part of the blackbody spectrum of the nuclear explosion. A blackbody is an object that absorbs all radiation and reflects none of it. When a nuclear detonation occurs, the resulting photons form a wavelength (λ) spectrum with intensity, or spectral radiance, I, based on Planck's equation,

$$I(\lambda) = \frac{2hc^2}{\lambda^5}\frac{1}{\exp[hc/\lambda kT]-1}, \tag{4}$$

where h is Planck's constant, c is the speed of light, k is the Boltzmann constant, and T is the temperature of the blackbody at thermal equilibrium. The equation can also be written in terms of frequency ν as

$$I(\nu) = \frac{2h\nu^3}{c^2}\frac{1}{\exp[h\nu/kT]-1}. \tag{5}$$

Between the extreme ultraviolet (EUV) and radio wavelengths, a blackbody curve can be used to fit the emission spectrum of the Sun, though the Sun is not a perfect emitter outside of this region, as shown in Figure 3.

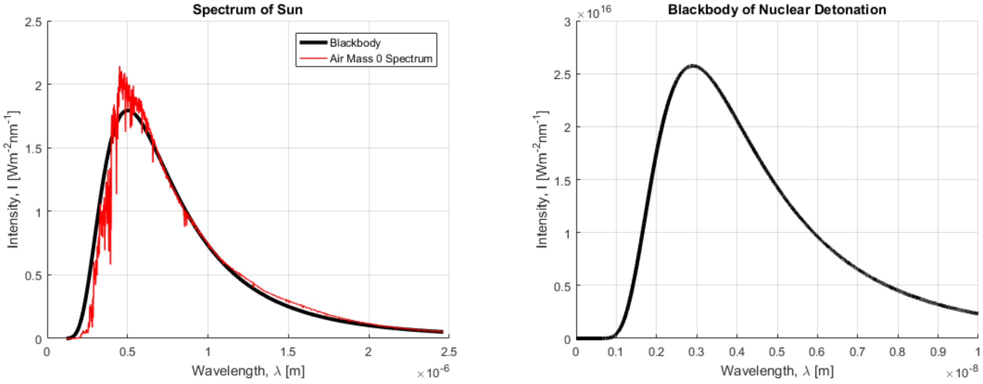

(a) (b)

Figure 3. These are example blackbody spectra of the Sun at 5778 K 3a and a nuclear detonation at 10^6 K 3b, estimated according to Wertz and Larson (2007). The red line in 3a is the 2000 American Society for Testing and Materials (ASTM) E-490 Air Mass 0 spectrum from the U.S. Department of Energy (DOE)/NREL/ALLIANCE, displayed to show that the Sun is not a perfect blackbody. Note that the axes are on different scales. The Sun peaks in the visible spectrum, whereas the nuclear detonation peaks in the EUV/x-rays.

The x-rays from the detonation then produce electrons through Compton scattering, bremsstrahlung radiation, the photoelectric effect, and fluorescence, whereas gamma rays will interact through Compton scattering, pair production, and the photoelectric effect. These electrons go on to create the EMP, damage electronics, create an aurora, and eventually form an artificial radiation belt.

2.1.2 Electromagnetic Pulse

When discussing HANDs, strategic analysts and members of the military are most concerned about the resulting EMP, an intense spike in electrical current and field produced by the products of fission. A pulse from a nuclear weapon detonated at high altitudes, defined as being above 30 km, can have an electric field magnitude of tens of thousands of volts per meter. This pulse propagates through the atmosphere to the ground, where it can disrupt power grids and microelectronics. An EMP from a HAND, called a high-altitude electromagnetic pulse (HEMP), can have effects spanning the width of the continental United States. Reports have found that a HEMP over the United States would be strong enough to cut most forms of communication including cell phones, radio, and above-ground telephone lines (Popik et al., 2017). Further, such a HEMP would short out or damage transformers in the power grid (Foster et al., 2008). If one transformer fails, its load is transferred to another transformer, which in turn fails and creates a cascading effect. Since the United States has no means to produce its own transformers, the cascading effect could cause large, extended blackouts that could cripple infrastructure. Hence, the United States government has called for repeated EMP commissions (Foster et al., 2008; Stuckenberg et al., 2018) and reports to determine the threat and response to such an attack. EMPs, however, are not unique to nuclear weapons. Lightning and solar storms can also produce EMPs, though nuclear detonations are different in that they have three distinct EMP stages, illustrated by Figure 4.

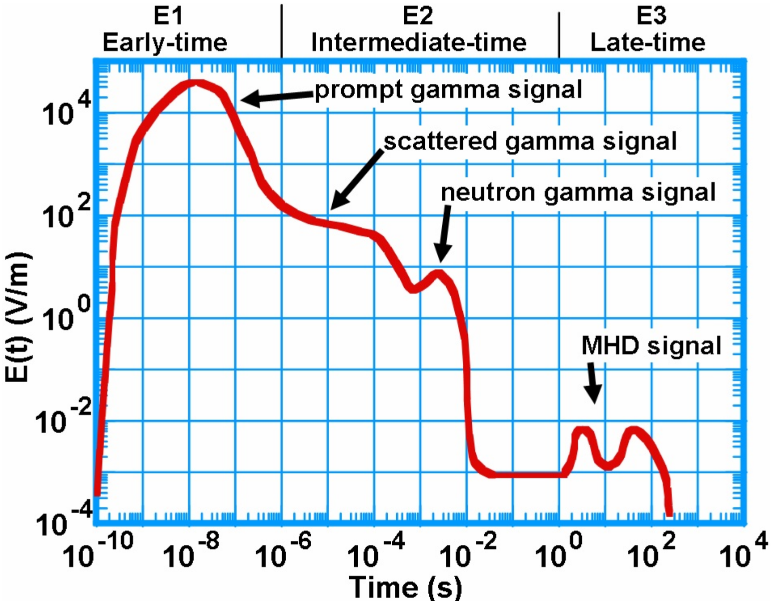

Figure 4. The EMP is divided into three main phases: E1, E2, and E3, with E3, or the MHD signal, being segmented into two separate phases. Each phase is caused by a different physical process and radiation source, and as such each phase has a distinct energy signature and timing. The graphic is courtesy of Popik et al. (2017).

E1 Phase.

In a high altitude nuclear detonation, a weapon will detonate at a height where the atmosphere is negligible. The gamma rays, which are emitted spherically in an exponentially rising pulse within tens of nanoseconds, disperse. Those that are directed toward the Earth eventually come to interact with the atmosphere at lower altitudes, where through Compton scattering they produce Compton electrons. In Compton scattering, the gamma ray will knock an electron found in an atom out of its orbit, freeing it, and impart energy to the electron in the form of kinetic energy. The electron is then scattered in a new direction, usually forward, while the gamma is deflected in the opposite direction. The region of interaction between gamma rays and atoms in the atmosphere is known as the source region. The Compton electrons produce a radial current with respect to the Earth's coordinate system.

These Compton electrons are then turned by the magnetic field around Earth, turning circularly with a radius known as the gyroradius or cyclotron radius, which is inversely proportional to the magnetic field strength:

$$r_c = \frac{mv_\perp}{|q|B}. \tag{6}$$

The electrons will come to a halt at the stopping distance, determined by the energy lost in collisions that produce secondary electrons. It takes 34 eV of energy to produce one electron-ion pair from these collisions after all ionization, and so each Compton electron produces about 30,000 electron-ion pairs (Longmire, 1978). The turning of the electrons produces a transverse current, while the resulting electrons from the ionization process form a conducting layer that will actually serve to shield some of the effects of the EMP. The current in turn generates an induced electric field, which propagates down to the Earths surface as an EMP. The fields from the E1 phase are illustrated in Figure 5. This ionizes almost the entire local atmosphere, which can cause ionospheric waves and drastically affect the chemistry of the region.

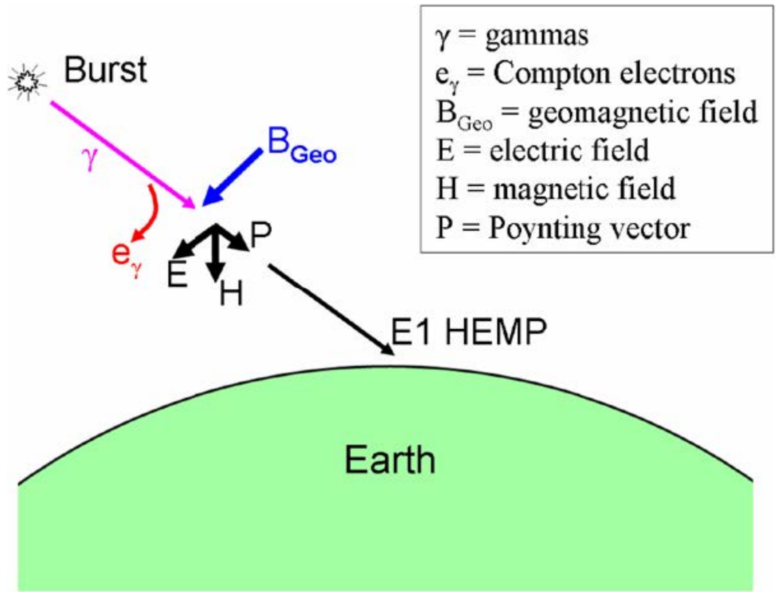

Figure 5. Above is a simplified diagram of the E1 phase of an EMP generated by a HAND. The gamma rays start at the point of detonation and through collisions produce Compton electrons, which are turned by the geomagnetic field. The turning produces currents and electric fields. This diagram was taken from Gombosi et al. (2017).

For a high-altitude burst, the area that the EMP affects is determined by the local magnetic field direction and the altitude of the burst. Typically, the electric fields will be distorted and will follow the field lines, forming the characteristic ”smile” plots, as seen in Figure 6, associated with a HAND where the currents and fields projected to the ground are distorted by the magnetic field to form a ”smile” instead of the expected circular pattern.

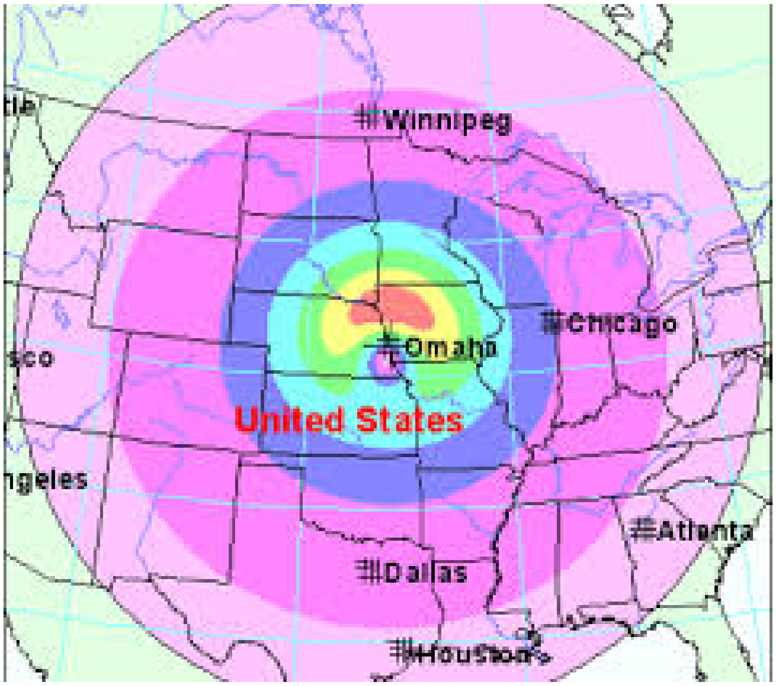

Figure 6. The characteristic "smile" plot of an EMP from a HAND. The propagating electric field is perturbed by the Earth's magnetic field lines and the curvature of the Earth (Defense Threat Reduction Agency, 2016).

E2 Phase.

Some fraction, 1/e or about 37%, of the gamma rays emitted from the detonation will interact with the atmosphere above the source region (Gombosi et al., 2017). As a result, there will be a time delay between when the prompt gamma rays arrive at the source region and when these delayed gamma rays arrive, as well as a small discrepancy in energy. These secondary gamma rays will interact similarly to the prompt gamma rays and will Compton scatter, producing another pulse similar to that in the E1 phase. However, the E2 phase will last up to 1,000 times longer than the E1 phase, while being weaker (Popik et al., 2017). This signal is further supplemented by the current produced from high energy neutrons that escape the blast, which eventually scatter inelastically at altitudes similar to the source region and produce gamma rays, which then Compton scatter at low altitudes. This causes replacement currents in the atmosphere and in the ground, which in turn produce both vertical electric fields from the Compton scattering and horizontal electric fields from the current in the ground since the ground is an imperfect conductor.

E3 Phase.

The x-rays emitted from the detonation will also spherically diverge from the point of detonation. Roughly half of these x-rays will travel downwards towards the ground and will be absorbed by the atmosphere above the source region. These x-rays will scatter a K-shell electron out of the atom, producing a photoelectron and a secondary x-ray from a higher-orbit electron filling the electron shell gap. The x-rays will cause an ionization cascade, which causes a heating of the higher altitude atmosphere. The heating and ionization, in turn, shields the ground from any signals from the blast region and locks in the magnetic field lines. Meanwhile, some of the fission fragments and the remaining weapon debris become highly ionized as a result of the detonation and are highly conductive as a result. The highly ionized elements are pushed upwards in altitude and push the geomagnetic field lines out of the region, creating a diamagnetic cavity. The expansion of the cavity is determined by the debris velocity and later by the altitude, eventually slowed by either atmospheric pressure or magnetic pressure. At large distances, the resulting cavity and deformation of the field lines can be approximated as a field-aligned dipole situated at the point of detonation and thus create electric and magnetic fields that can exist for longer than E1 and E2 and cover an even wider area. This is called the blast phase, shown in Figure 7, and usually only occurs if the detonation took place above 100 km.

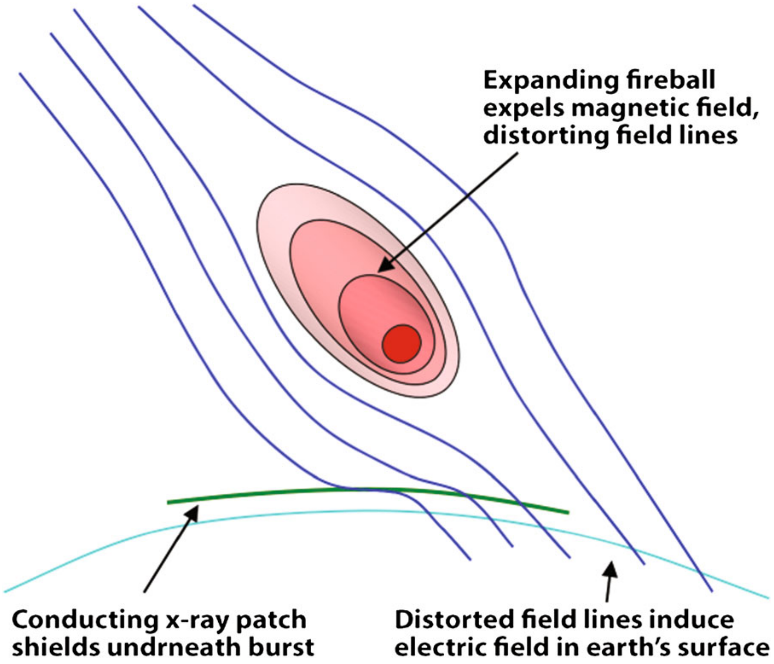

Figure 7. During the E3 phase, the x-rays released from the HAND will cause an ionization cascade and heat the atmosphere. Meanwhile, the fission fragments will be shot upwards and will push the geomagnetic field lines out, creating a diamagnetic cavity. This cavity acts as a field-aligned dipole that creates a farther-reaching effect. Figure courtesy of Gombosi et al. (2017).

The remaining debris and fission fragments, along with ions heated by the shock, travel down along the geomagnetic field lines. At altitudes under the point of detonation, the energy will be deposited similarly to other phases, and the deposition will heat and ionize the atmosphere. Typically, this will be in the *E*-region of the ionosphere. There is additional heating from EUV radiation. The atmosphere will first expand and then start to buoyantly rise as it becomes increasingly conductive. The rising conductive layer then crosses the geomagnetic field, inducing a current through the dynamo effect. The current from the dynamo flows to the west, with northern and southern return currents at the edges of the buoyant region. This causes a two-cell current system that induces an electric field oriented in the same direction and propagates to the ground, as illustrated in Figure 8. This is known as the heave phase and only occurs for blasts above 150 km. It is more localized than the blast phase.

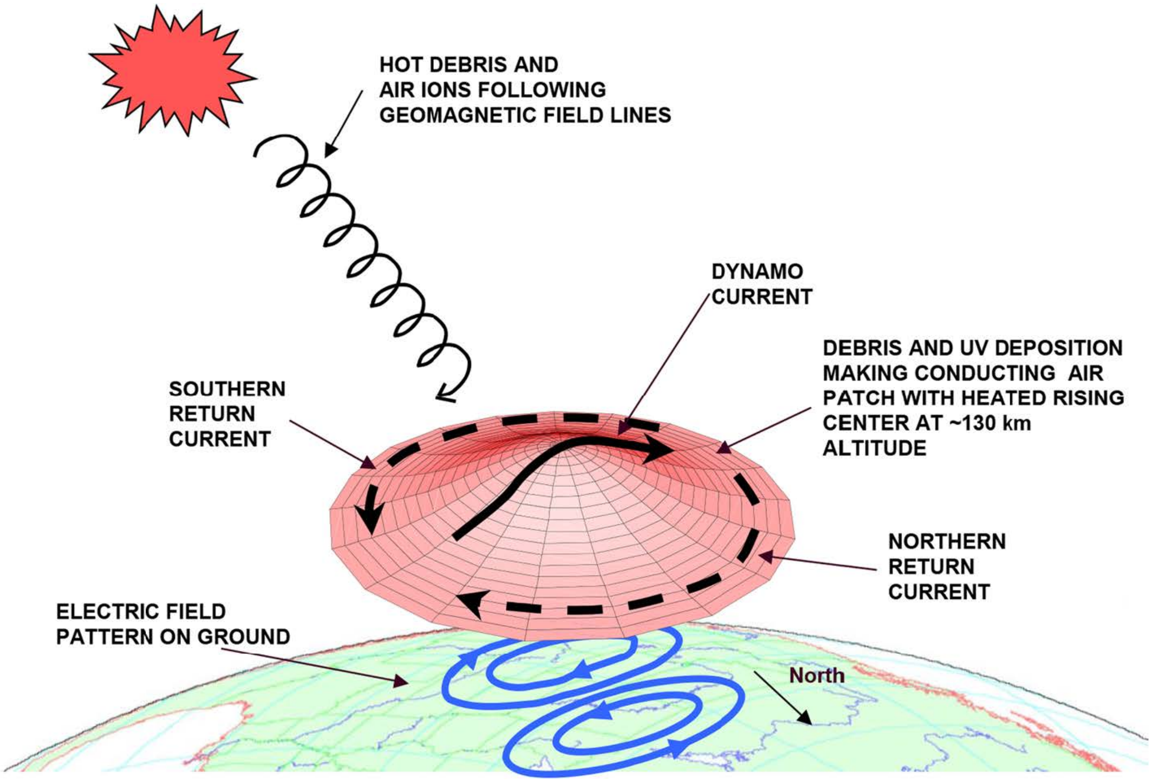

Figure 8. As the atmosphere under the HAND heats, the atmosphere will expand and then buoyantly rise. The layer will be extremely conductive. As the layer rises and crosses the geomagnetic field lines, the dynamo effect will induce a current. This image was taken from Gombosi et al. (2017).

2.2 Earth's Radiation Environment

The upper atmosphere of Earth, where ionization occurs and plasma is present, is called Earth's radiation environment. The terrestrial ionosphere is a region of Earth's atmosphere above the troposphere and stratosphere, usually starting in the mesosphere between 40 km and 100 km depending on the reference, and extending up to roughly 1,000 km into the thermosphere and exosphere (Pisacane, 2016). The ionosphere is said to be the lower bound of the magnetosphere. It is characterized by the significant number of free electrons and accompanying ions which form a plasma layer. Figure 9 shows the stratification of the layers of the atmosphere. Historically, scientists have known about interactions in the upper atmosphere for millennia through the existence and observation of aurorae. However, the ionosphere as a layer was not hypothesized until the 1800s when Carl Gauss and Balfour Stewart theorized the existence of electric currents in the atmosphere (Schunk and Nagy, 2009). Then, in 1902, Arthur E. Kennelley and Oliver Heaviside predicted that there was a highly conductive region in the atmosphere, termed the "Heaviside layer", to explain Guglielmo Marconi's radio transmissions, which were the first evidence of the layer (Russel et al., 2016). The existence was finally verified in 1924 when the first accepted measurements were taken by Gregory Breit and Merle A. Tuve in the U.S. and Edward V. Appleton and M. A. F. Barnett in the United Kingdom (Schunk and Nagy, 2009).

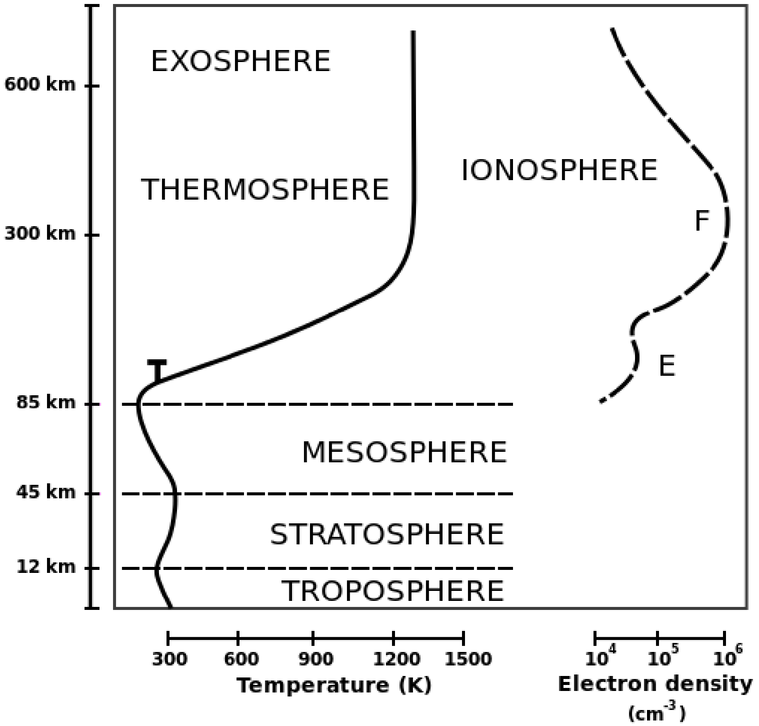

Figure 9. The ionosphere is distinguished from the atmosphere by its temperature and its electron density. It is a part of the thermosphere, situated above the troposphere, stratosphere, and mesosphere, but below the magnetosphere and protonosphere. Figure public domain, courtesy of Bhamer.

The ionosphere is divided into main three regions: the *D*-region, *E*-region, and the *F*-region, with the *F*-region being split into the F_1-region and F_2-region during the daytime, since the ionizing light creates two distinct electron density peaks; at night, however, the ionization processes stop and the two *F*-regions merge. The regions are distinguished from each other by the peak electron densities as a variation of height, as can be distinguished in the electron density profiles in Figure 10. The different regions have been shown to have different transport mechanisms and drivers, as discussed in the relevant subsections.

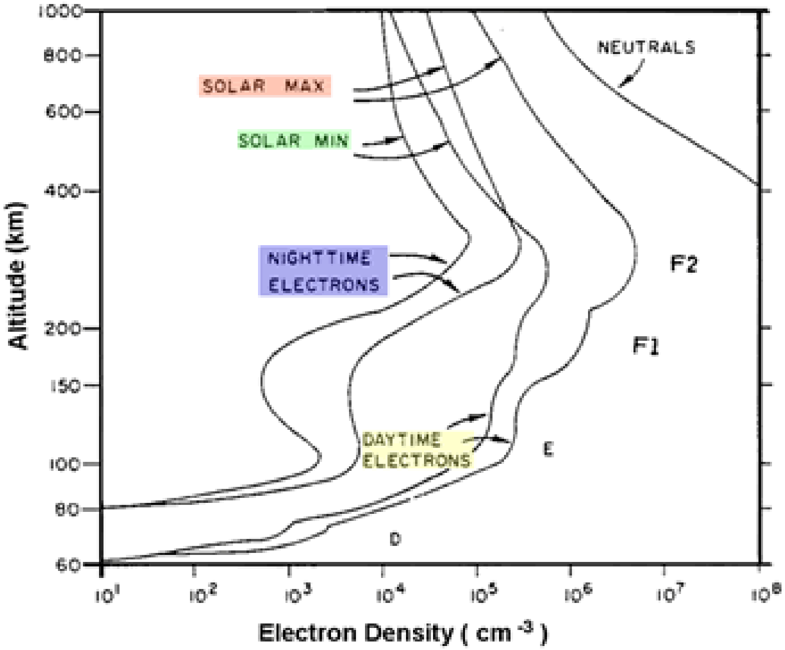

Figure 10. The ionosphere is subdivided into four regions: the *D*-region is the lowest, followed by the *E*-region, the F_1-region, and the F_2-region. The ionosphere is separated by electron density peaks, determined by varying physical mechanisms. Figure courtesy of Peter Guest at the Naval Postgraduate School, Department of Meteorology.

2.2.1 *D*-Region

The *D*-region of the ionosphere is the lowest region, located between approximately 40 km to 95 km. This region is heavily driven by hard x-rays with wavelengths between 0.1-1 nm and by Lyman α radiation with a wavelength of 121.5 nm (Pisacane, 2016). These radiation regimes ionize N_2, O_2, O, and NO. The major ion species that result from the ionization are NO^+ and O_2^+. These ion species cause hydration in this region, which cause water cluster ions and cause three-body chemical reactions (Schunk and Nagy, 2009). Further, negative ions can be found in this region, further complicating the chemistry. This region essentially disappears at night, but during the day the electron number density (N_e) can be on the order of magnitude of 10^9 m^{-3} (Pisacane, 2016).

2.2.2 *E*-Region

The first observed layer of the ionosphere was the E-region. Directly above the D-region, it extends from 95 km to 150 km. In this region, soft x-rays with wavelengths from 1-10 nm ionize N_2, O_2, O, and NO, while ultraviolet radiation from approximately 80 nm to 102.7 nm ionizes O_2 that combines with nitrogen to create NO^+ (Pisacane, 2016). The E-region can be well modeled by production and recombination mechanisms, and has a distinct peak at about 120 km; this peak shifts upwards in altitude at night. Typically, the E-region has an N_e of 10^{11} m^{-3} (Pisacane, 2016) but with a neutral density of 10^{17} m^{-3} (Schunk and Nagy, 2009), which makes this region weakly ionized. It is also known for the sporadic-E phenomena.

2.2.3 *F*-Region

Above the E-region is the F-region, extending from 150 km to approximately 1,000 km. The F-region is ionized by EUV radiation in the regime of 10-100 nm, which ionizes atomic oxygen and, at higher altitudes, H and He (Pisacane, 2016). This region splits into two distinct regions during the day: the lower region, the F_1-region, is typically found between 150 km and 250 km and is driven by some chemical reactions and some transport mechanisms (Schunk and Nagy, 2009) with an N_e between 2-5 $\times 10^{11}$ m^{-3} (Pisacane, 2016); the F_2-region extends into the protonosphere and exhibits the ionization maximum, where the transport mechanisms are balanced by the chemical losses. The peak value normally occurs between 300 km and 350 km and has an N_e of 10^{12} m^{-3} during the day, but an order of magnitude less at night (Pisacane, 2016). The region above the F_2-region peak is referred to as the topside ionosphere. The difference between the F_1-region and the F_2-region during the day results from decrease in recombination coefficient for the chemical reactions as the altitude increases.

2.2.4 Van Allen Radiation Belts

A particle with a nonzero charge entering an axially symmetric magnetic field with varying field strength that forms a magnetic mirror will display three types of motion, as illustrated in Figure 11: cyclotron motion around the field lines, bouncing motion along the field lines, and the slow drift motion around the axis of symmetry.

Cyclotron motion, also called gyration, is a result of a particle in motion in a magnetic field. If a particle of mass m and charge q is moving with a velocity of $\vec{v} = \vec{v_\perp} + \vec{v_\parallel}$ with respect to the magnetic field $\vec{B}$, the particle will move in a circular path through the magnetic field with a radius equal to the gyroradius given by Equation 6 and with a cyclotron frequency given as:

$$\omega_c = \frac{|q|B}{m}. \tag{7}$$

The bounce motion of the particle occurs when the field strength varies along the magnetic field lines. A particle trapped in this configuration will bounce at turning points determined by the strength of the magnetic field and the initial velocity vector. To determine if a particle has been trapped, it is useful to calculate the pitch angle α, which is the angle between the velocity vector of the particle and the the magnetic field. The minimum pitch angle α_0, where any value below α_0 results in the particle being lost, is defined using the minimum magnetic field strength B_0 and the maximum magnetic field strength that occurs at the mirror points, $B_{\max}$:

$$\sin^2 \alpha_0 = \frac{B_0}{B_{\max}}. \tag{8}$$

Drift motions, meanwhile, are slower in comparison to bounce and cyclotron motions. Drift motions occur when a second force perpendicular to the magnetic field is applied to a particle. In relation to particles in the upper atmosphere, the two drift

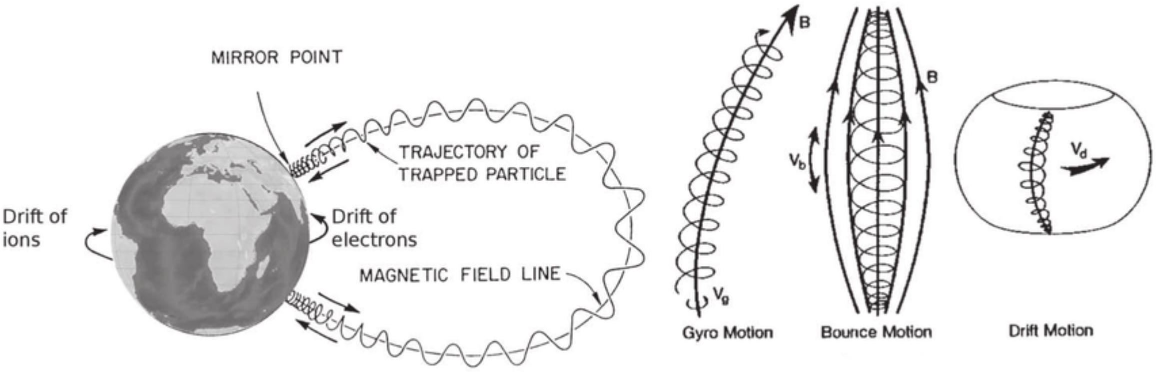

Figure 11. Particles in the Van Allen radiation belts undergo three types of motion: gyration, bounce, and drift. The combination of all three motions creates a trapped radiation environment with energetic, charged particles. Figures from Regi (2016) with kind permission of Societá Italiana di Fisica.

motions that contribute most to the motion of the particles are the gradient drift (Pisacane, 2016), shown in Figure 12a,

$$\vec{v_G} = \frac{mv_\perp^2}{2qB}[\frac{\hat{B} \times \vec{\nabla} B}{B}] = \frac{mv_\perp^2}{2qB^3}\vec{B} \times \vec{\nabla} B, \tag{9}$$

and the curvature drift (Pisacane, 2016), shown in Figure 12b,

$$\vec{v_{cf}} = \frac{mv_\parallel^2}{qB}[\frac{\hat{B} \times \hat{R_C}}{R_C}] = \frac{mv_\parallel^2}{qB^3}\vec{B} \times \vec{\nabla} B, \tag{10}$$

where R_C is the radius of curvature (Gurnett and Bhattacharjee, 2017).

Since both drift motions are dependent on the sign of the charge, electrons will move opposite of protons and other positively charged ions and thus create a current. The longitudinal drift of ions and electrons around the globe is called the ring current.

The combination of these three types of motion around Earth result in belts of trapped radiation. These belts were first verified in 1958 by Explorer I with a simple Geiger counter, and named the Van Allen radiation belts in honor of the principle

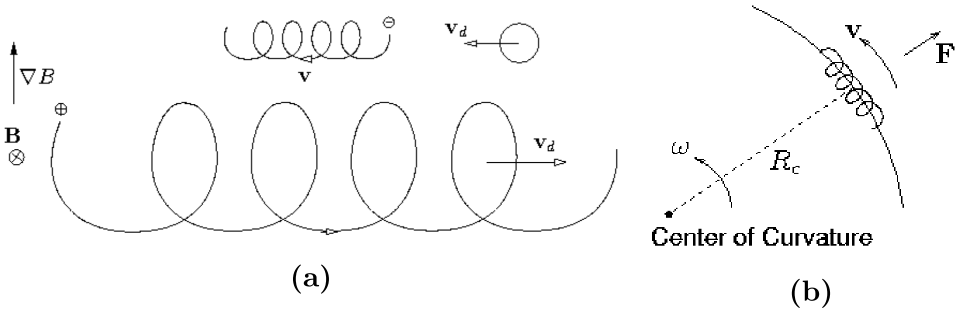

Figure 12. Simple illustrations of the gradient drift (12a) and the curvature drift (12b) of a particle. This motion results from the guiding center of the particle's motion inside a non-uniform magnetic field. Figures adapted from Hutchinson (2001).

physicist, James Van Allen, who hypothesized and proved their existence (Pisacane, 2016). These belts carry charged particles around the globe and can deposit them in the upper polar latitude atmosphere. The belts are characterized in terms of the energy of their trapped particles and their distance from Earth, described by the McIlwain L-shell parameter (Morrow, 2014),

$$L = \frac{r}{R_E \sin^2 \theta}. \tag{11}$$

Here, r is the radial distance from the center of the Earth, R_E is the radius of the Earth, and θ is the angle measured from the pole to r.

Recent satellite missions have revealed the presence of three distinct radiation belts, though one is only apparent in times of significant storming (Baker et al., 2013). The other two are referred to as the "inner" and "outer" belts, and exhibit a distinct gap region between them. The inner Van Allen belt is found approximately between 1.1 and 2.5 Earth radii (7,016 km to 15,945 km) and the outer belt is found between 3 and 6 Earth radii (19,134 km to 38,268 km). Typically, the inner belt contains electrons with energies less than 1 MeV and most of the high-energy protons, while the outer belt, which is correlated to the solar wind, has energies of approximately 2

MeV (Gombosi et al., 2017). The fluxes corresponding with the various energies are highly dependent on the solar and geomagnetic conditions, but are typically fairly low for quiet conditions and not a significant threat to hardened electronics on satellites that may operate in or near these regions. However, this changes if a significant amount of high-energy electrons or ions are introduced to the belts.

2.3 Ionospheric Models

The ionosphere has a considerable effect on day-to-day operations on Earth. Radio waves propagate by bouncing off the lower ionosphere. GPS is also affected by the ionosphere through scintillation, refraction, dispersion, and other effects, which cumulatively are the source of the greatest error in timing and precision (Codrescu, 2007). As a consequence, many agencies are interested in developing a model of the ionosphere to nowcast and forecast the changes in TEC, peak frequency of the E-region (foE), peak electron density of the E-region (nmE) or F_2-region (nmF2), and peak altitude of the E-region (hmE) or F_2-region (hmF2). Several common models that are important historically and operationally will be discussed in the following subsections.

2.3.1 Chapman Model

The simplest model of the ionosphere is the Chapman model. Developed by Sydney Chapman in 1931 (Chapman, 1931), this model assumes monochromatic light is entering a plane-parallel atmosphere of one absorbing species at an angle less than about 85°, depicted in Figure 13. It also assumes that the concentration of the absorbing species varies with altitude by a constant characteristic length, known as the scale height, H, and that the species has an absorbing cross section, σ_a that is independent of altitude. From Schunk and Nagy (2009), letting n be the number density of the absorbing species at an altitude z and χ be the solar zenith angle measured from the vertical, the neutral number density is defined as

$$n(z) = n(z_0)\exp[-\frac{(z - z_0)}{H}], \tag{12}$$

where z_0 is an arbitrary reference height. If m is the mean mass of a molecule of the absorbing species, T is the temperature of the absorbing species, and g is the acceleration due to gravity, and assuming that temperature and gravitational acceleration do not noticeably change with altitude, then the scale height H for the absorbing species is

$$H_s = \frac{kT}{mg}. \tag{13}$$

Finally, denoting the unattenuated photon flux at the top of the ionosphere as I_∞, the photon flux at an altitude z can be written as

$$I(z, \chi) = I_\infty \exp[-Hn(z)\sigma_a \sec\chi]. \tag{14}$$

However, this equation does not take into consideration that the there is a wavelength dependence for the absorption cross section and the unattenuated photon flux. It also does not consider multiple species (denoted by s) or the inherent dependence of temperature and gravitational acceleration on altitude. Taking this into consideration, the new equations for scale height, number density, and photon flux are:

$$H_s(z) = \frac{kT_s(z)}{m_s g(z)} \tag{15}$$

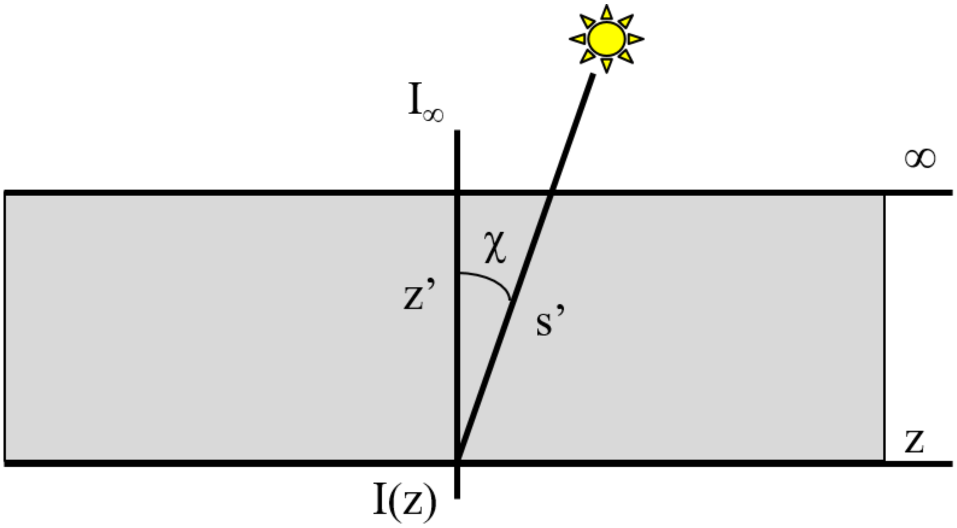

Figure 13. This is a simplified illustration of the Chapman model for the ionosphere. This assumes a source at an altitude of infinity above the surface with one species and monochromatic light. The unattenuated photon flux, described as the photon flux at infinite altitude, is I_∞, while at an altitude z it is $I(z)$. The photons travel along a path of length s', with a vertical distance of z' and a solar zenith angle of χ.

$$n_s(z) = n_s(z_0) \exp T_s(z_0) T_s(z) \exp[-\int_{z_0}^{z} \frac{dz*}{H_s(z*)}] \tag{16}$$

$$I(z, \lambda, \chi) = I_\infty(\lambda) \exp[-\int_{\infty}^{z} \sum_s n_s(z) \sigma_s^a(\lambda) ds'], \tag{17}$$

where s' is the optical path of the photons. This leads to a common parameter known as the optical depth, τ:

$$\tau(z, \lambda, \chi) = \int_{\infty}^{z} \sum_s n_s(z) \sigma_s^a(\lambda) ds'. \tag{18}$$

With the probability of the absorption of a photon that results in an ion-electron pair symbolized as η, the Chapman production function to describe the rate of production of electrons P_c is thus written as

$$P_c(z,\chi) = I_\infty \eta \sigma_a n(z) \exp[-Hn(z)\sigma_a \sec\chi]. \tag{19}$$

The peak production rate can be found through differentiation, and the altitude of the maximum $z_{\max}$ and the maximum production rate are found to be

$$z_{\max} = z_0 + H \log[n(z_0) H \sigma_a \sec\chi] \tag{20}$$

$$P_c(z_{\max},\chi) = \frac{I_\infty \eta \cos\chi}{H} e^{-1}. \tag{21}$$

Although the Chapman model is fairly basic, it does work as an approximation for the E-region and the F_1-region, but fails for the D-region and F_2-region, as the D-region is dominated by chemical processes and the F_2-region is dominated by transport mechanisms. Most ionospheric models build off this simple model and add complexity, including having several absorbing species, transport mechanisms, and temperatures influenced by chemical reactions, in addition to other physics.

2.3.2 EUVAC

Even though it is not an ionosphere model, it is worth discussing the EUVAC model. The EUV flux model for aeronomic calculations (EUVAC) was designed to model the solar EUV flux since the Sun is not a perfect blackbody, detailed in Richards et al. (1994). This model has been incorporated into many ionospheric models to simply calculate various parameters such as ionization rates and unattenuated photoelectron fluxes. The model relies on the input of the daily average solar radio flux at 10.7 cm, called the F10.7 index and measured in units of [$\times 10^{-22}$ W Hz^{-1}m^{-2}], or solar flux units (sfu), and the 81-day average of the F10.7 index, <F10.7>. The combination of these factors is combined into a simple factor,

$$P = \frac{\mathrm{F10.7} + < \mathrm{F10.7} >}{2}. \tag{22}$$

The EUVAC model uses 37 wavelength intervals from 5 nm to 105 nm, based on measurements from the EUVS instrument on the Atmospheric Explorer E satellite (Schunk and Nagy, 2009). These intervals are associated with a modified reference flux, called F74113, and a scaling factor A for the interval, which are included in Table **??** in the Appendix. The unattenuated flux for each interval i is empirically calculated by

$$I_i = \mathrm{F74113}_i[1 + A_i(P - 80)]. \tag{23}$$

The model has been updated for newer measurements, and newer models have been made for higher resolutions, but EUVAC remains heavily ingrained with more sophisticated ionospheric models.

2.3.3 NeQuick

Slightly more complex than the Chapman model are the quick-run models of the ionosphere. These models are designed to be computationally inexpensive and are empirically-based climatological models. One such model, used extensively by the European Space Agency (ESA) and other international collaborations, is NeQuick, a three-dimensional, time dependent model. Specific details are further explained in documentation by the European Commission (2016). It was developed by the Aeronomy and Radiopropagation Laboratory, now T/ICT4D Laboratory, of the Abdus Salam International Centre for Theoretical Physics in Trieste, Italy, with the collaboration of the Institute for Geophysics, Astrophysics and Meteorology of the University of Graz in Austria, and is now in its second iteration. The description of the new version (Nava et al., 2008) uses a modified G. Di Giovanni and S. M. Radicella (DGR) model for the profile from 90 km up to the F_2-region peak, which includes five semi-Epstein layers. The bottomside and topside of the ionosphere are determined by different modeled semi-Epstein layers. The topside of the model can extend up into the Van Allen radiation belts, extending to 25,000 km, but NeQuick does not consider the interactions of the magnetosphere or radiation belts. The model requires the inputs of position of interest, time, and either the F10.7 value or the sunspot number, which can be computed empirically from the F10.7 index. It outputs the electron number density.

2.3.4 USU-GAIM

Utah State University's Global Assimilation of Ionospheric Measurements (USU-GAIM) is a data assimilation model of the ionosphere built upon the physics-based Ionosphere Forecast Model. From Zhu et al. (2006), the Ionosphere Forecast Model is a three-dimensional, high-resolution, multi-ion global model that can extend from 90 km in altitude to 1,600 km in altitude, with the vertical profiles being variable in refinement. Its spatial resolution is variable, but the finest resolution is 2° latitude and 5° longitude. The temporal resolution is also variable, being able to scale down to 5 minute increments. The Ionosphere Forecast Model numerically solves the equations for continuity, momentum, and energy for multiple ion species along magnetic field lines for plasma flux tubes. It focuses on five ion species: NO^+, O_2^+, N_2^+, O^+, and H^+. It also includes processes for field-aligned diffusion, cross-field electrodynamic drifts, thermospheric wind, compositional changes, energy-dependent chemical reactions, ion production from EUV and from auroral precipitation, thermal conduction, diffusion-thermal heat flow, local heating and cooling effects, and pole displacement. The model requires the inputs of neutral composition, neutral wind, the $\vec{E} \times \vec{B}$ field, EUV radiation, and precipitation and convection at latitudes greater than ±60°. Specifically, according to the CCMC, it requires the F10.7 index, the 81-day average of the F10.7 index, the daily Ap index, and eight 3-hour Kp indices. Outputs include three-dimensional number density distributions of the ions and electrons, ion and electron temperatures, TEC, nmE, nmF2, hmE, and hmF2, plus other additional plasma parameters.

GAIM, which builds off of the physics-based model, comes in two different packages: GAIM Gauss-Markov (GAIM-GM) and GAIM Full Physics (GAIM-FP). GAIM-FP has evolved to use the Ionosphere-Plasmasphere Model instead of the IFM, but both use a Kalman filter for the data assimilation. Currently, GAIM-GM is employed both at the Air Force Weather Agency and at NASA's CCMC. Due to the availability of GAIM-GM over GAIM-FP, GAIM-FP will not be discussed here despite it being the only current model looking to incorporate *D*-region chemistry. According to the working paper by Scherliess et al. (2017), GAIM-GM uses various ionospheric measurements to correct the predictions of the Ionosphere Forecast Model, using the Kalman filter techniques to incorporate the data and the Gauss-Markov process to evolve the deviations and error covariances over time. It is limited in altitude to between 92 km and 1,400 km, with a set vertical resolution of 4 km in the *E*-region and 20 km in the *F*-region and above. The global resolution is also less refined than the Ionosphere Forecast Model, with 4.6° resolution in latitude and 15° resolution in longitude. When run on the CCMC, the only input parameters necessary are the start date for the time of interest and the duration, as the other parameters are looked for automatically through available databases.

2.3.5 GITM

The University of Michigan also developed a physics-based model of the ionosphere, the Global Ionosphere-Thermosphere Model, or GITM, which is detailed in Ridley et al. (2006). This model uses a stretched three-dimensional spherical grid, where the longitude resolution is fixed but the latitude and altitude resolution can be non-uniform. It is also different from other ionospheric models as it uses an altitude-based vertical grid based on scale height instead of a pressure-based vertical grid that other models use. It also does not assume hydrostatic equilibrium when solving the dynamics equations, solves for advection and chemistry explicitly, and includes nine neutral species (O, O_2, $N(^2D)$, $N(^2P)$, $N(^4S)$, N_2, NO, H, and He) and nine ion species ($O^+(^4S)$, $O^+(^2D)$,$O^+(^2P)$, O_2^+, N^+, N_2^+, NO^+, H^+, and He^+). It also has the option to incorporate the International Geomagnetic Reference Field (IGRF) model for variable magnetic fields, and GITM is further coupled to many high-latitude ionospheric electrodynamic models that can be chosen depending on the system of interest, and it has options for data assimilation. Of note is that heating in GITM is determined by solar and Joule heating, and heat from excitation is not calculated. The model available on the CCMC has a longitudinal resolution of 5° and a latitudinal resolution of 2.5°, and an altitude range between 90 km and 600 km. Similar to other models, it requires an input for the F10.7 index but not the 81-day average, as well as needing the hemispheric power index (HPI), interplanetary magnetic field (IMF) parameters, and solar wind velocity. In return, it outputs neutral wind velocity, temperature, number density, and mass density; ion temperature and number density; electron temperature and number density; and plasma velocity.

2.3.6 SAMI3

The cleverly-named Sami3 is Also a Model of the Ionosphere (SAMI3) was developed at the Naval Research Laboratory as a three-dimensional physics-based ionospheric model, based on SAMI2 (Sami2 is Also a Model of the Ionosphere), which was a two-dimensional model. Its strength is in its chemical calculations; according to Huba et al. (2017), SAMI3 models the plasma and chemical evolution of seven ion species: NO^+, O_2^+, N_2^+, O^+, N^+, H^+, and He^+. This includes twenty-one chemical reactions and radiative recombinations. It solves temperature equations for electrons and the H^+, He^+, and O^+ ions. It also includes ion inertia in the ion momentum equations along the magnetic field, and it uses the $\vec{E} \times \vec{B}$ drift for transverse motion. It has an altitude range of 85 km to 20,000 km, but since the ionosphere is calculated as a complete flux tube, is latitudinally limited to between ±62.5° about the magnetic equator. The CCMC cites that the neutral composition and temperature are determined from the empirical NRLMSISE-00 (Naval Research Laboratory, mass spectrometer and incoherent scatter radar, extending through the exosphere, released in 2000) model while the neutral winds are from the empirical Horizontal Wind Models (HWMs). The model requires the F10.7 index and the 81-day average F10.7 index, the Ap index, and the $\vec{E} \times \vec{B}$ drift velocity. It outputs the ion density, temperature, and velocity; the electron density and temperature; TEC; nmF2; and hmF2. It also has options for incorporation into models like TIE-GCM.

2.3.7 TIE-GCM

The last model to be discussed here is the Thermosphere-Ionosphere-Electrodynamics General Circulation Model (TIE-GCM) developed at the High Altitude Observatory (HAO) at the National Center for Atmospheric Research (NCAR). This model is another three-dimensional physics-based ionospheric model with options for data assimilation. It is non-linear and focuses on the coupling of the thermosphere and ionosphere and the self-consistent solutions of the low-latitude electric fields, further detailed in Qian et al. (2013). For high latitudes, it relies on either the Heelis potential or the Weimer empirical potential. To solve the equations of continuity, momentum, and energy, it uses explicit fourth-order centered finite difference for the horizontal component. It also employs a Shapiro filter to smooth the solutions. It includes the evolution of five neutral species (NO, $N(^4S)$, $N(^2D)$, O, and O_2) with an option for He and with CO_2 being specified through diffusive equilibrium (Foster, 2016), and it includes calculations for five ion species: O^+, O_2^+, N_2^+, NO^+, and N^+. TIE-GCM has multiple options for auroral forcing to drive the polar regions; various options for the magnetic field parameters, including using the IGRF model; and options for solar forcing, making it highly versatile. Since the model is based on a pressure grid, its altitude range is dependent on solar conditions but is typically between 97 km and 700 km. The longitudinal and latitudinal resolutions are 5°, but this can be refined to 2.5°. It requires an input of the F10.7 index, the 81-day average F10.7 index, the 3-hour Kp index, and specifications for either the Heelis or Weimer potential. It can produce outputs for ion and electron number densities; neutral mass-mixing ratios; ion, neutral, and electron temperatures; neutral wind velocities; pressure surfaces; and electric potential.

III. Methodology

Overview

This chapter details how the study was conducted. It first started with a cursory examination and comparison of multiple physics-based models to understand their limitations and to create an operational range before modification. From these results, one model, TIE-GCM, was chosen to attempt to modify to incorporate a HAND. A quick-run empirical model, NeQuick, was used to test the modification of the F10.7 index before the modification was computed for TIE-GCM. The next step was to modify TIE-GCM to incorporate a localized F10.7 index and then to reflect the significant temperature changes from a HAND. Finally, the results were compared to data from Starfish Prime and to comparable geomagnetic storming events.

3.1 Comparing Models

The study started with an examination of the different ionospheric models to determine which would be robust enough to modify. To begin with, the models were chosen from NASA's CCMC website (`https://ccmc.gsfc.nasa.gov/requests/requests.php`), as the models available there can be run on request. Though there are many models available on the CCMC website, only four were chosen due to their operational or research use and availability of the source code: USU-GAIM, GITM, SAMI3, and TIE-GCM. With the run-on-request feature, a user can choose the input parameters for the models. The maximum and minimum values for the F10.7 index, 81-day average F10.7 index, and the Ap index/Kp values/HPI (depending on the model specifications) were used to determine the extreme cases for the models in order to determine how variable the models were to an event like a HAND and to see how responsive the models were to variations in solar activity. The solar activity serves here as a proxy for the enhancement in ionization due to a HAND. The comprehensive list of parameters and chosen values is given in Table 3. The maximum and minimum values for these variables are determined by the CCMC developers. These extremes were then compared to real ionosonde data for the day and time of choice taken from the Digital Ionogram Database (DIDBase), compiled by the Global Ionospheric Radio Observatory (GIRO) (Reinisch and Galkin, 2011), to see if there was a significant change between maximum and minimum input parameters. The exception is USU-GAIM, which searches for the input parameters automatically based on the chosen date, with no option for modification on the request run page.

The date chosen was 9 July 2012, the 50th anniversary of the Starfish Prime test, as the date range for the models on CCMC is limited to 1994 and later. The F10.7 index on this date was 179.6 sfu, with an 81-day average of 137.6 sfu, an Ap index of 42 nT, a Kp index of 47, an interplanetary magnetic field (IMF) strength in the x-direction (B_x) of 1.2 nT, IMF strength in the y-direction (B_y) of -0.4 nT, and IMF strength in the z-direction (B_z) of -8.3 nT, all taken from OMNI 2 satellite data and the historical database from Space Weather Canada.

Table 3. These are the model parameters entered into NASA's CCMC run on request feature for each model for a minimum/maximum comparison. F10.7 is the solar activity in the 10.7 cm radio band; <F10.7> is the 81-day average; HPI is the hemispheric power index; Ap is a measure of geomagnetic activity; B$_x$, B$_y$, and B$_z$ are measures of the IMF strength; v$_x$ is the solar wind velocity; and ρ_{sw} is the solar wind density.

	GITM	SAMI3	TIE-GCM
Maximum	F10.7 = 200 sfu, HPI = 10, B_x = 0 nT, B_y = 0 nT, B_z = -4 nT, v_x = 400 km/s	F10.7 = 200 sfu, <F10.7> = 200 sfu, Ap index = 30 nT, sinusoidal model, $\vec{E} \times \vec{B} = 30$ m/s	F10.7 = 200 sfu, B_x = 0 nT, B_y = 0 nT, B_z = -4 nT, v_x = 400 km/s, $\rho_{sw} = 60$ cm^{-3}
Minimum	F10.7 = 70 sfu, HPI = 1, B_x = 0 nT, B_y = 0 nT, B_z = -4 nT, v_x = 400 km/s	F10.7 = 70 sfu, <F10.7> = 70 sfu, Ap index = 0 nT, sinusoidal model, $\vec{E} \times \vec{B} = 5$ m/s	F10.7 = 70 sfu, B_x = 0 nT, B_y = 0 nT, B_z = -4 nT, v_x = 400 km/s, $\rho_{sw} = 4$ cm^{-3}

To compare the data, specific locations were chosen to compare electron density profiles. These locations were chosen based on ionogram data available for the date. Of these locations, three were selected to represent the equatorial ionosphere, mid-latitude ionosphere, and polar ionosphere, as the ionospheric physics for each region is significantly different. The complete network of ionosondes are displayed in Figure 14, which was current as of 2014. The Ramey ionosonde was chosen for the equatorial ionosphere, located at the geographic location of 18.50° latitude and 292.90° longitude. The mid-latitude station was located at Idaho National Laboratory, found at 43.81° latitude and 247.32° longitude. Finally, the polar ionosphere region was represented by the Qaanaaq station at 77.50° latitude and 290.80° longitude.

Figure 14. The locations of all existing and planned ionosondes that contribute to the GIRO DIDBase. Ramey is located in Puerto Rico, Idaho National Laboratory in Idaho in the continental U.S., and Qaanaaq is in Greenland. Figure courtesy of GIRO DIDBase.

From the results, the models were characterized by strengths and weaknesses and the differences quantified by the mean squared error. The mean squared error (MSE) is an estimator of the difference between a sets of data. Since the electron density profiles are not distributions and are not normally distributed, distributional tests would not provide a good indicator of change between models. Further, as the models and the ionogram do not have stated variances or uncertainties, a χ^2 goodness-of-fit test cannot be used either. The MSE provides an approximate comparison, where if the number of elements in a data set is n and the two sets are denoted as S_1 and S_2 respectively, then the MSE is computed as

$$MSE = \frac{1}{n}\sum_{i=1}^{n}(S_{1_i} - S_{2_i})^2. \tag{24}$$

The lower the MSE, the closer the two data sets are to each other, whereas the larger the MSE, the more different the two sets are. The MSE was computed to quantify the differences between the models and the ionogram data, and then between the two extreme cases for each model.

TIE-GCM was chosen to be modified due to its results in the comparison, its strengths concerning differentiating the polar latitudes from the equatorial and mid-latitudes, its fine resolution, its source code availability, and its ability to incorporate global datasets, such as IGRF.

3.2 Modifying Models

The next step in the process was to determine if any ionospheric models would accurately capture the effects of a HAND when the source code was modified. First, NeQuick, a quick-run model, was used to see the effects of a drastically increased global F10.7 index, using the indices of 200 sfu, 500 sfu, 1,000 sfu, and 1,500 sfu. Since the default NeQuick model limits the F10.7 index to 193 sfu, a modified version courtesy of Dr. Sean Elvidge at the University of Birmingham was used. The NeQuick model was then adjusted to ingest an array of F10.7 indices for each set of geographic coordinates to form a grid of F10.7 indices. This allowed for the specification of a localized event within the NeQuick framework. The location of the event was chosen to be at 0.00° latitude and 0.00° longitude at 0000 Coordinated Universal Time (UTC) to best showcase the propagation on the global map and because most HAND tests were done at night. The F10.7 index was only raised at the event location. It was then attenuated by the square of the distance r,

$$\text{F10.7} = \frac{\text{F10.7}_{\text{source}}}{r^2}, \tag{25}$$

to simulate the divergence of the weapon's effects. Given that the Earth is curved and that the model relied on geographic coordinates, the distance in the model was calculated using the Haversine formula for a rough approximation. Considering two sets of coordinates in latitude and longitude, (ϕ_1, λ_1) and (ϕ_2, λ_2), the distance d between the points is calculated by

$$d = 2R_E \arcsin[\sqrt{\sin^2(\frac{\phi_2 - \phi_1}{2}) + \cos\phi_1 \cos\phi_2 \sin^2(\frac{\lambda_2 - \lambda_1}{2})}]. \tag{26}$$

At this point, it was necessary to determine how to translate the parameters from a nuclear weapon into something usable by the ionospheric models. The F10.7 index is not based on the blackbody spectrum of the Sun; it is a proxy for solar activity based on one radio emissions line that corresponds with fluctuations in the EUV spectrum and with sunspot number. It is a measured flux on Earth, measured at one station in Canada. The F10.7 index was also not designed to indicate anomalous solar activity, such as flares, as it is a daily average. The F10.7 index, instead, is used because it corresponds directly to both sunspot number and to the average EUV flux of the Sun. In order to avoid having to recalculate all the parameters that are derived from the F10.7 index, it was decided to estimate the EUV flux associated with a HAND using Planck's equation for a blackbody. Since the EUVAC model converts the F10.7 index and the 81-day average to EUV fluxes, the process was reversed, and the HAND EUV spectrum was binned according to the bins of the EUVAC model and the corresponding F10.7 index backed out from the calculations. The temperature of the fireball, estimated from Wertz and Larson (2007) as 10^6 K, was used as the blackbody temperature and as the resulting temperature for the neutrals, ions, and electrons in this region.

Once the technique was shown to have a result with NeQuick, it was decided to repeat a similar procedure with a physics-based model: TIE-GCM. First, the F10.7 index was increased to 200 sfu, 500 sfu, 1,000 sfu, and 1,500 sfu. Then, a supplemental module was written to include parameters for using the script (a 0/1 selection), the radius of a fireball, the temperature of the fireball, the location of the detonation, and the altitude at which it was detonated, which was added to the input file seen in Figure 38. These parameters were then used to recreate the F10.7 index for a detonation and then diverge it across the globe, creating an array of F10.7 indices. This required modifying the source codes to have the functions that use the F10.7 index to pull the value for the correct coordinate. The source files that are the primary users of the F10.7 index are the chem.F file, which calculates the chemical reaction rates; the qrj.F file, which utilizes the EUVAC model; and the settei.F file, which calculates the electron and ion temperatures. This did not provide a comprehensive picture of the enhancement due to a HAND. Then, the temperature was modified within the source files to reflect the heat generated by the fireball. The temperature was first attenuated using the inverse square law, but this did not accurately reflect the dissemination of heat in the atmosphere since at high altitudes, the energy from the fireball would not be absorbed as quickly as at lower altitudes. As a first order approximation, the temperature was attenuated by a fraction of 1/100 over an area of radius of 1,000 km, where then after it was attenuated according to the inverse square law. However, this resulted in the model crashing from the high temperatures, so the radius was reduced to 500 km, but this also was too much for TIE-GCM so it was reduced to 100 km. The complete list of modified files in TIE-GCM is provided in Table 6 in Appendix A.

3.3 Validation of Model with Data

The final step was to check the results with the available observational data. Given that the last high-altitude tests were conducted in 1962, there is little data available concerning the effect on the lower ionosphere. However, there is data from the satellites in orbit at the time of detonation or closely after Gombosi et al. (2017). The data from the satellites were in terms of omnidirectional counting rates or omnidirectional fluxes. The flux values were converted to approximate densities using the average velocity of a particle in orbit. NeQuick has features that allow it to extend the altitude to several Earth radii away. This enabled a comparison for the lower Van Allen belt enhancement, though the ionospheric models do not include mechanisms for the Van Allen belts. The lower belt enhancement provided an upper bound for what should be seen by the models.

The data was also compared to the March 2013 geomagnetic storm, which was studied by Yue et al. (2016) and includes both the satellite data and the results of the TIE-GCM model of the event. This comparison was completed by comparing the maximum changes in the differential TEC between the March 2013 event and the maximum changes from the TIE-GCM trials conducted in this study.

IV. Results

Overview

This chapter presents the results of the study and discusses their significance. The results are first displayed for the comparison study between models on the CCMC website and the actual ionosonde data. Next, the calculations performed by NeQuick for both the global F10.7 index and the localized array of F10.7 indices will be presented. This is followed by the results from the modification of TIE-GCM, and is concluded by the comparison to Starfish Prime data and the data from the March 2013 geomagnetic storm.

4.1 Model Comparison

The study began by comparing the chosen models available on NASA's CCMC website with the ionograms of the data from GIRO. The data was pulled from DIDBase and is displayed in Figure 15, though only the ionograms from Ramey (Fig. 15a), Idaho National Laboratory (Fig. 15b), and Qaanaaq (Fig. 15c) were used for comparison to demonstrate the different latitudinal regions of the ionosphere.

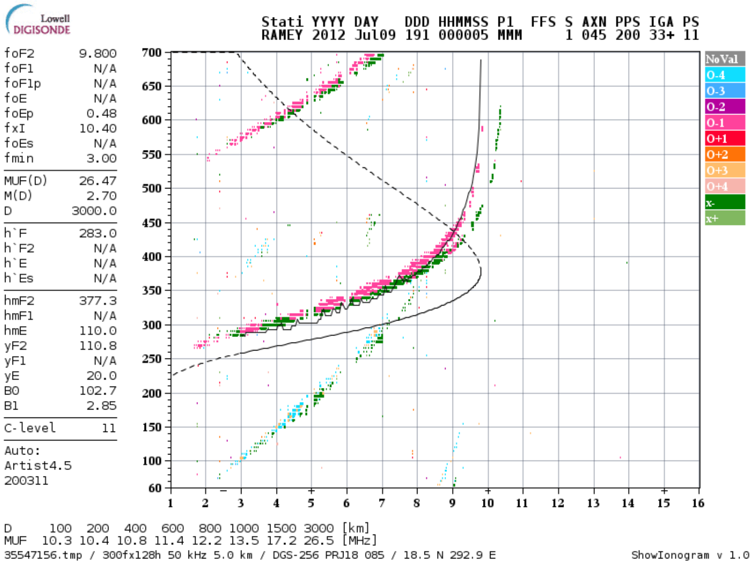
Lowell DIGISONDE
Stati YYYY DAY DDD HHMMSS P1 FFS S AXN PPS IGA PS
RAMEY 2012 Jul09 191 000005 MMM 1 045 200 33+ 11
foF2 9.800
foF1 N/A
foF1p N/A
foE N/A
foEp 0.48
fxI 10.40
foEs N/A
fmin 3.00
MUF(D) 26.47
M(D) 2.70
D 3000.0
h`F 283.0
h`F2 N/A
h`E N/A
h`Es N/A
hmF2 377.3
hmF1 N/A
hmE 110.0
yF2 110.8
yF1 N/A
yE 20.0
B0 102.7
B1 2.85
C-level 11
Auto:
Artist4.5
200311
NoVal
O-4
O-3
O-2
O-1
O+1
O+2
O+3
O+4
x-
x+
D 100 200 400 600 800 1000 1500 3000 [km]
MUF 10.3 10.4 10.8 11.4 12.2 13.5 17.2 26.5 [MHz]
35547156.tmp / 300fx128h 50 kHz 5.0 km / DGS-256 PRJ18 085 / 18.5 N 292.9 E
ShowIonogram v 1.0

(a)

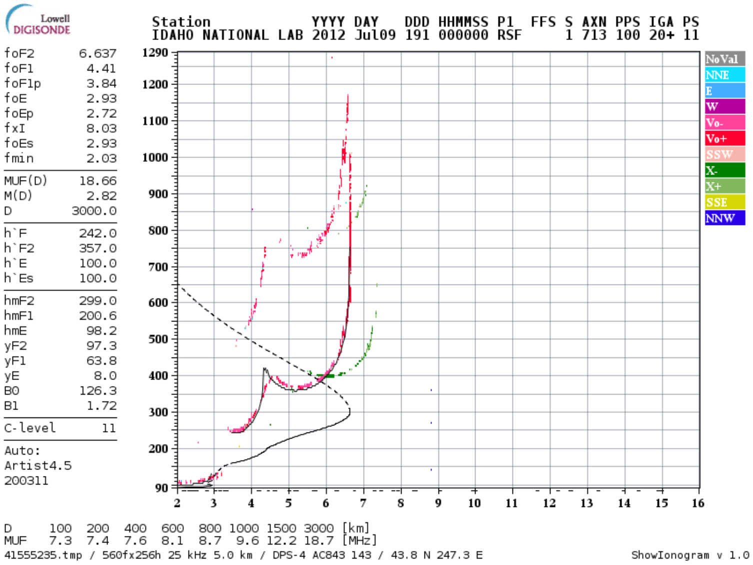
Lowell DIGISONDE
Station YYYY DAY DDD HHMMSS P1 FFS S AXN PPS IGA PS
IDAHO NATIONAL LAB 2012 Jul09 191 000000 RSF 1 713 100 20+ 11
foF2 6.637
foF1 4.41
foF1p 3.84
foE 2.93
foEp 2.72
fxI 8.03
foEs 2.93
fmin 2.03
MUF(D) 18.66
M(D) 2.82
D 3000.0
h`F 242.0
h`F2 357.0
h`E 100.0
h`Es 100.0
hmF2 299.0
hmF1 200.6
hmE 98.2
yF2 97.3
yF1 63.8
yE 8.0
B0 126.3
B1 1.72
C-level 11
Auto:
Artist4.5
200311
NoVal
NNE
E
W
Vo-
Vo+
SSW
X-
X+
SSE
NNW
D 100 200 400 600 800 1000 1500 3000 [km]
MUF 7.3 7.4 7.6 8.1 8.7 9.6 12.2 18.7 [MHz]
41555235.tmp / 560fx256h 25 kHz 5.0 km / DPS-4 AC843 143 / 43.8 N 247.3 E
ShowIonogram v 1.0

(b)

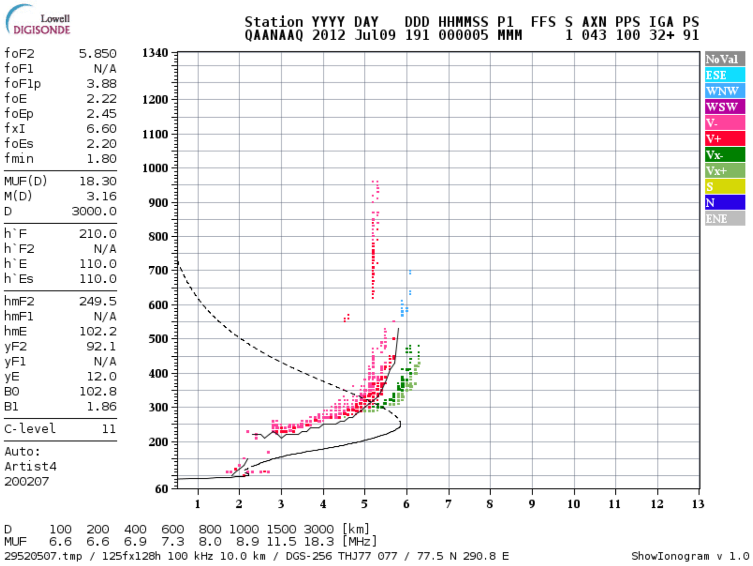

(c)

Figure 15. These ionograms are the observed data from the GIRO ionosondes, described in Reinisch and Galkin (2011). The ionosonde at Ramey (Fig. 15a) is in the equatorial region, while Idaho National Laboratory (Fig. 15b) is mid-latitude and Qaanaaq (Fig. 15c) is in a polar region. The red data are the ordinary waves, while the green are the extraordinary waves. The important parts of the figures are the black curves, which are the ionospheric profiles drawn by the ARTIST program. The solid black line indicates the bottomside ionosphere whereas the dotted black line is the extrapolated topside ionosphere.

From the runs-on-request, the electron density and altitude data for the various models were found at the geographic coordinates of the ionosondes using the maximum and minimum parameters from Table 3, displayed in Figure 16. There are many interesting phenomena to note about these electron density profiles: in the equatorial plot (Fig. 16a), the minimum parameters create F_2-region peaks that are lower in altitude than for the maximum parameters, which lead to the electron densities for the minimum parameters being higher than for the maximum parameters at altitudes between the E-region peak and the F_2-region peak. However, the maximum parameters yield higher densities at higher altitudes. Further, SAMI3 does not produce data for the polar region exhibited by Figure 16c since it calculates its results from a single flux tube, which limits it in latitude.

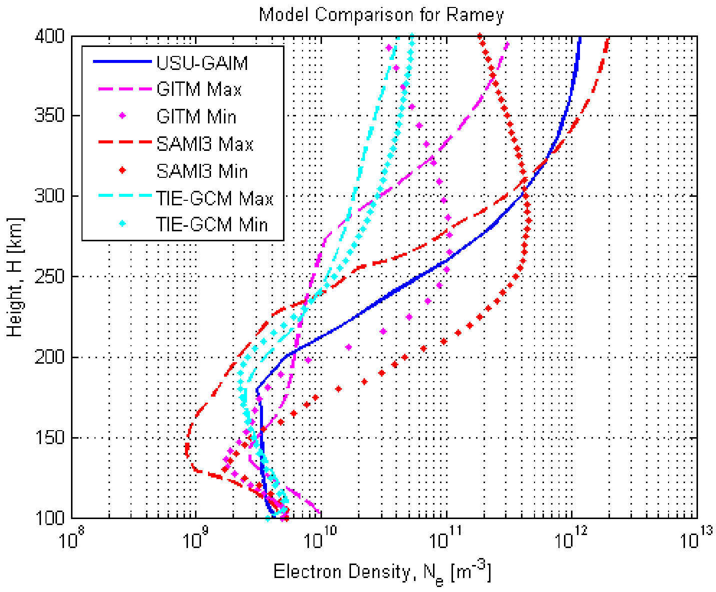
Model Comparison for Ramey
USU-GAIM
GITM Max
GITM Min
SAMI3 Max
SAMI3 Min
TIE-GCM Max
TIE-GCM Min
Height, H [km]
400
350
300
250
200
150
100
10^8
10^9
10^{10}
10^{11}
10^{12}
10^{13}
Electron Density, N_e [m^{-3}]

(a)

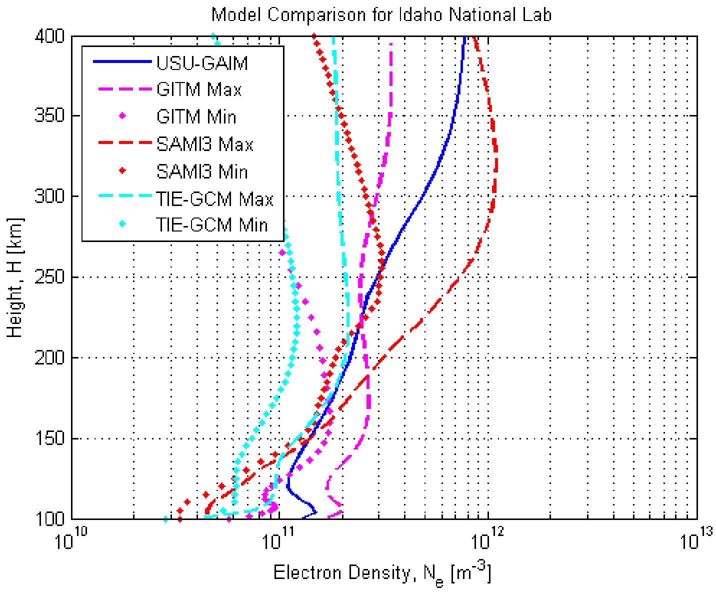
Model Comparison for Idaho National Lab
USU-GAIM
GITM Max
GITM Min
SAMI3 Max
SAMI3 Min
TIE-GCM Max
TIE-GCM Min
Height, H [km]
400
350
300
250
200
150
100
10^{10}
10^{11}
10^{12}
10^{13}
Electron Density, N_e [m^{-3}]

(b)

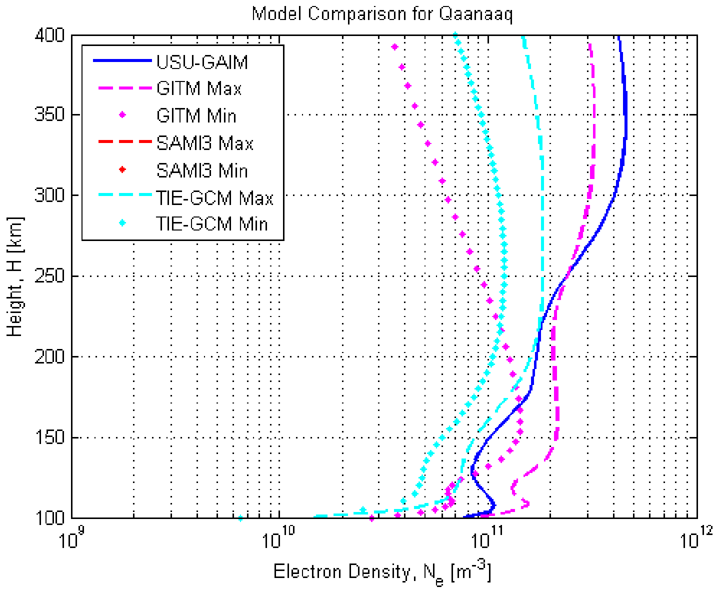

(c)

Figure 16. These plots of the electron density were created from the results from NASA's CCMC runs on request, including the results from USU-GAIM, GITM, SAMI3, and TIE-GCM. The minimum and maximum values for the model parameters were used, as described in Table 3. The same locations as the ionosondes were used, though these plots are for the electron density and not the frequency. The dashed lines are for the maximum parameters and the dotted lines are the minimum parameters. USU-GAIM did not have options for parameters and is represented by the solid line.

For a direct comparison between the ionosonde data and the results from the runs-on-request, the electron density was converted into the plasma frequency:

$$f_p = \frac{1}{2\pi}\sqrt{\frac{N_e q_e^2}{m_e \epsilon_0}}, \tag{27}$$

with q_e being the charge of an electron, m_e the mass of an electron, and ϵ_0 being the permittivity of free space. This was then plotted and displayed with the ARTIST profile from the ionograms, shown in Figure 17. The results from the models were compared to the ionogram curve using the mean squared error (MSE) to give an idea of which model run had the greatest variation from the ionogram data. The MSE was also found between the minimum parameter runs and the maximum parameter runs. Both results are displayed in Table 4.

Table 4. The mean squared error is indicative of how well the model results align with the measured data interpolated by the ARTIST program in the ionogram, as well as how well the minimum and maximum parameter runs compared to each other. The equatorial runs correspond to the ionosonde at Ramey, the mid runs to the ionosonde at Idaho National Laboratory, and the polar to the ionosonde at Qaanaaq.

Model Run	MSE with Ionogram	MSE with Min/Max
USU-GAIM, Equatorial	0.4338	-
USU-GAIM, Mid	0.8954	-
USU-GAIM, Polar	1.5314	-
GITM Maximum, Equatorial	9.6872	1.2274
GITM Minimum, Equatorial	15.5240	1.2274
GITM Maximum, Mid	1.1387	2.9072
GITM Minimum, Mid	7.8024	2.9072
GITM Maximum, Polar	1.0744	3.0070
GITM Minimum, Polar	4.9258	3.0070
SAMI3 Maximum, Equatorial	1.6275	13.5421
SAMI3 Minimum, Equatorial	8.4754	13.5421
SAMI3 Maximum, Mid	3.9262	11.6737
SAMI3 Minimum, Mid	2.3155	11.6737
SAMI3 Maximum, Polar	-	-
SAMI3 Minimum, Polar	-	-
TIE-GCM Maximum, Equatorial	22.0632	0.0460
TIE-GCM Minimum, Equatorial	20.1427	0.0460
TIE-GCM Maximum, Mid	2.9581	1.3504
TIE-GCM Minimum, Mid	7.9154	1.3504
TIE-GCM Maximum, Polar	1.4327	0.6041
TIE-GCM Minimum, Polar	3.5465	0.6041

As expected, the USU-GAIM model best matched the observed data for the day, time, and location except for the polar region, but SAMI3 showed the most range between minimum and maximum parameters. TIE-GCM showed the least difference between maximum and minimum. Neither GITM nor TIE-GCM overestimated the frequency, even with the maximum parameters chosen. This is indicative that GITM and TIE-GCM are more heavily influenced by the IMF field strength and its effects on Earth's currents than on solar activity. SAMI3 displays the most variation since it is heavily reliant on chemistry, which is primarily driven by solar activity.

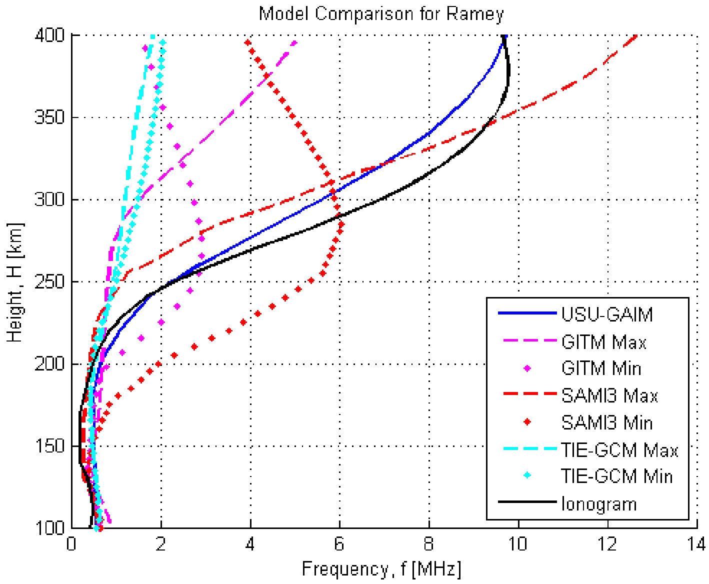

(a)

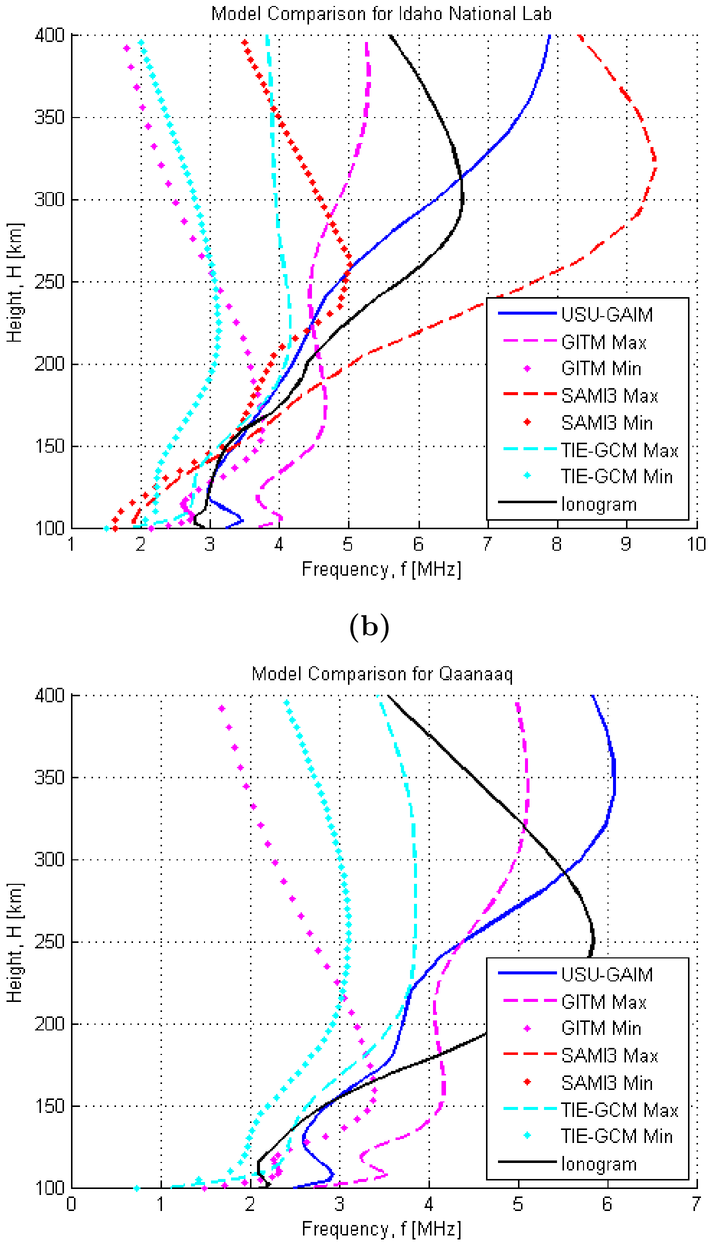

(b)

(c)

Figure 17. The electron densities from the models were converted to frequencies and plotted with the interpreted profile displayed in the ionogram drawn by the ARTIST program. The ionosonde data is represented by the black curve. The maximum model parameters are again shown by dashed lines, with dotted lines for the minimum and a solid blue line for USU-GAIM.

4.2 Modified Models

4.2.1 Modified NeQuick.

Once the models from CCMC were compared, the influence of extreme F10.7 indices was investigated using NeQuick. The first study, presented in Figure 18, used an F10.7 index of 200 sfu. The results were displayed as a hmF2 map, a nmF2 map, a TEC map, and electron density profiles, shown collectively at the end. The hmF2 map shows the variation in the altitude of the ionosphere, while the nmF2, TEC, and electron density profiles demonstrate how much the electron content changes as solar activity is increased. The TEC maps are in units of TEC units (TECU), which are $\times 10^{16}\text{m}^{-2}$. The resulting plots indicate what would be expected from a day with high solar activity during a typical maximum of the solar cycle. This is close to NeQuick's normal maximum of 193 sfu, so it is to be expected that there are no drastic variations and thus, this can be used as a baseline for higher values of F10.7.

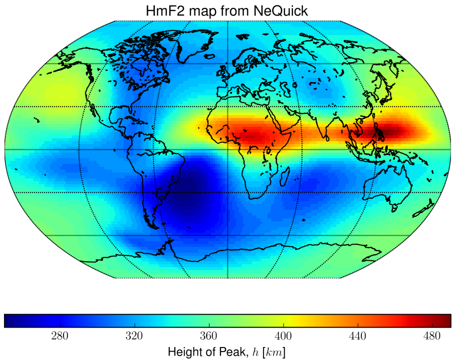

(a)

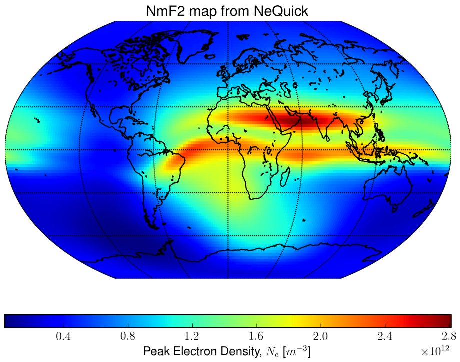

(b)

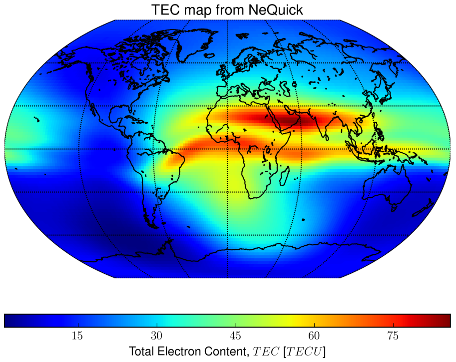

(c)

Figure 18. The hmF2 (Fig. 18a), nmF2 (Fig. 18b), and TEC (Fig. 18c) maps for a global F10.7 index of 200 sfu in NeQuick. The results are very similar to what the results would be on a day of slightly high solar activity, as an F10.7 index of 200 sfu is just above the normal range of values.

Next, the F10.7 index was increased to 500 sfu, with the results shown in Figure 19. There is a drastic increase in the height of the F_2-region peak (Fig. 19a), though it is most pronounced over the eastern hemisphere, which corresponds to the daytime side of the planet. This is also reflected in the TEC map (Fig. 19c). These results are not physical, as the ionosphere would not extend up to 2,500 km.

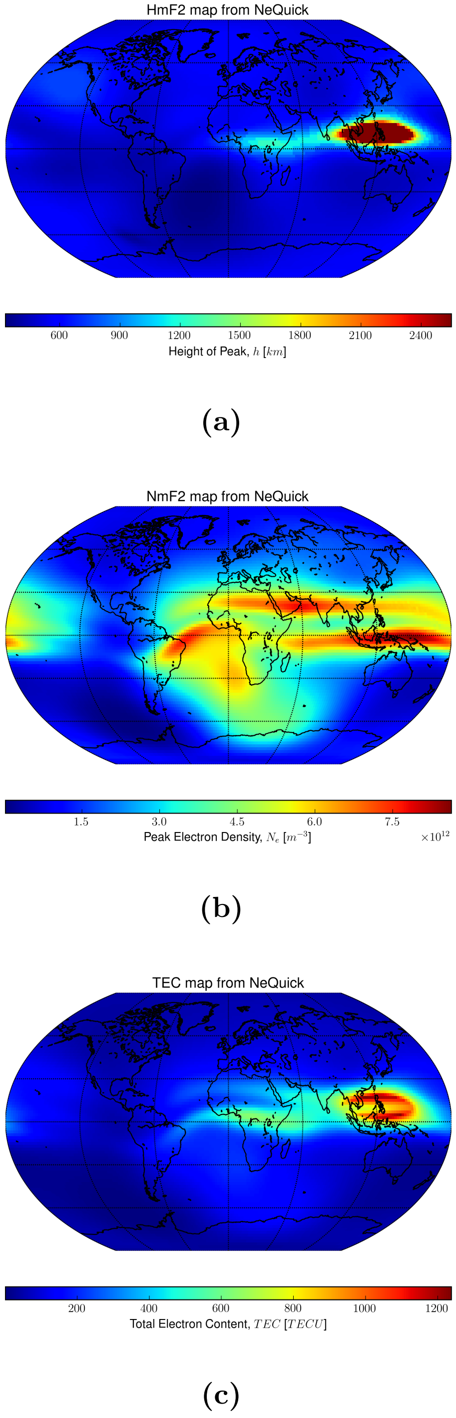

Figure 19. The hmF2 (Fig. 19a), nmF2 (Fig. 19b), and TEC (Fig. 19c) maps for a global F10.7 index of 500 sfu in NeQuick. The color scale here is considerably different from that in Figure 18. Since the F10.7 index is more than twice what it would be on a standard day, the electron densities are far higher, as is the height of the F_2-region peak.

As the F10.7 index is increased to 1,000 sfu (Fig. 20), the maximum peak of the F_2-region (Fig. 20a) does not increase, but instead more of the values of hmF2 are raised to the maximum altitude of about 2,500 km. The electron density at the F_2-region peak (Fig. 20b) is now an order of magnitude higher than when F10.7 was 200 sfu, while the TEC (Fig. 20c) is two orders of magnitude higher.

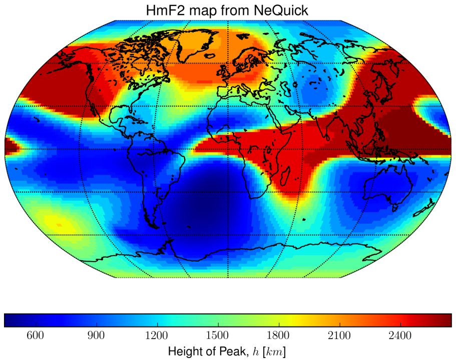

(a)

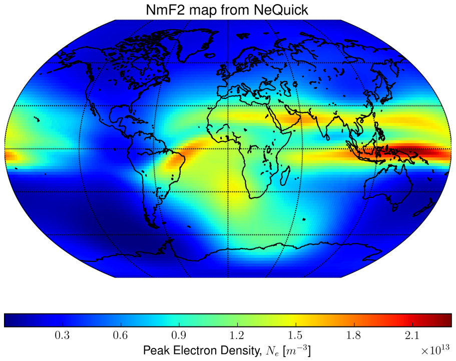

(b)

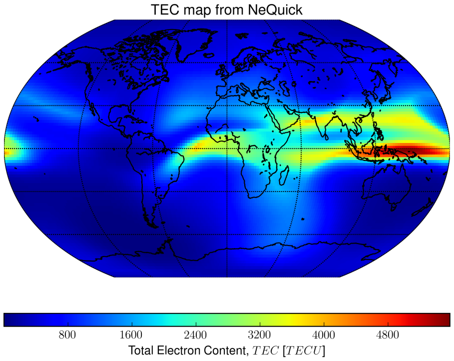

(c)

Figure 20. The hmF2 (Fig. 20a), nmF2 (Fig. 20b), and TEC (Fig. 20c) maps for a global F10.7 index of 1,000 sfu in NeQuick. The F10.7 index here is completely unphysical, as is evident by the resulting map of hmF2 and the values of the electron densities and TEC.

Lastly, in Figure 21, the F10.7 index was driven to 1,500 sfu. This is a completely unrealistic value, but shows the point at which the entire globe is affected by the solar activity, even on the night side. The TEC and peak F_2-region altitudes are extreme and the region of enhancement around the geomagnetic equator spans almost all the way around the globe.

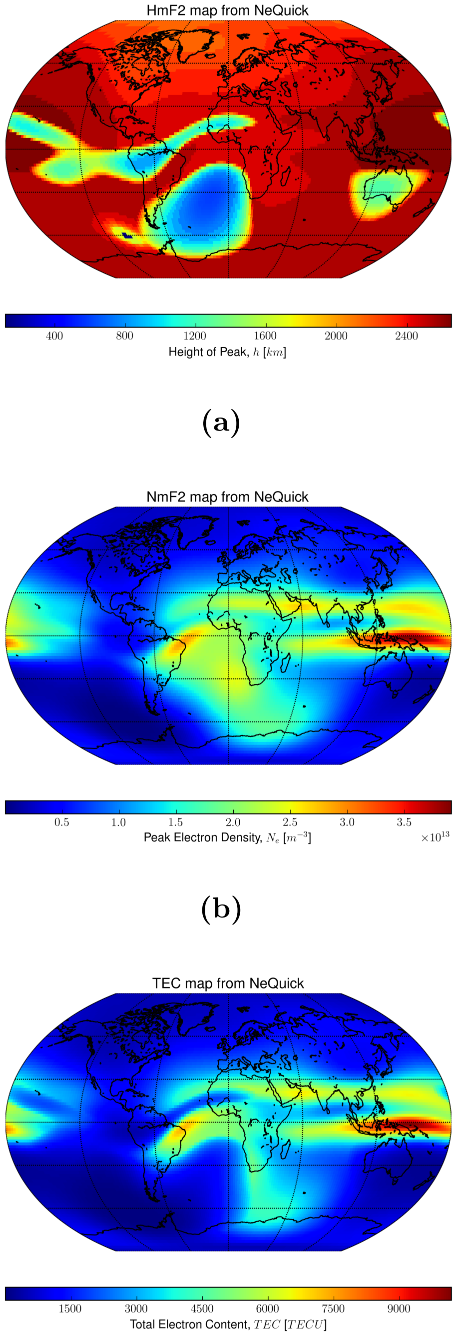

(a)

(b)

(c)

Figure 21. The hmF2 (Fig. 21a), nmF2 (Fig. 21b), and TEC (Fig. 21c) maps for a global F10.7 index of 1,500 sfu in NeQuick. This is an extreme case for F10.7, but shows how much the electron content is affected by the F10.7 index and solar activity.

Once NeQuick demonstrated what an extreme F10.7 index would look like if propagated around the globe, the F10.7 was recalculated with the EUVAC model using parameters for a HAND. An array of F10.7 indices at each geographic coordinate was made, assuming the F10.7 index at the point of detonation would attenuate as the inverse of the square of the distance. Assuming that the temperature of the fireball was 10^6 K, an estimate from Wertz and Larson (2007), and the radius of the fireball is 600 m, the resulting F10.7 index for a nuclear detonation was found to be 8.5186×10^5 sfu. The F10.7 index for the HAND was then attenuated by the inverse square law and run again in NeQuick, resulting in the data shown in Figure 22. Since the grid was only refined to 2° in latitude and longitude, the F10.7 index diverges rapidly in terms of pixels, so the only enhancement shown from the HAND is in the pixel containing the detonation, at 0° latitude and longitude. The maps (Fig. 22a, 22b, and 22c) indicated that elsewhere, the ionosphere resembles that at the actual F10.7 value of 179.6 sfu, which was the measured F10.7 value on that day. The electron density profiles in Figure 23 support this.

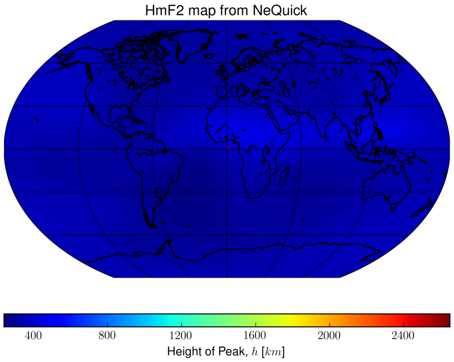

(a)

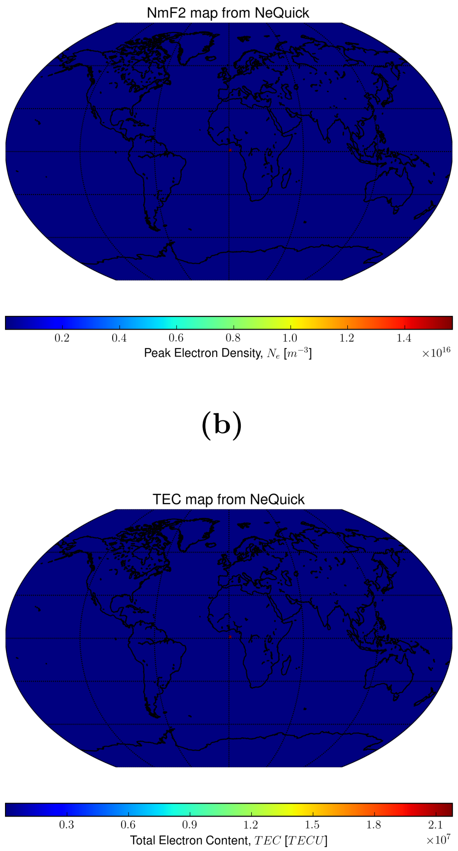

(b)

(c)

Figure 22. Lastly, the hmF2 (Fig. 22a), nmF2 (Fig. 22b), and TEC (Fig. 22c) maps from NeQuick if an array of F10.7 indices is formed using the EUVAC model and diverges from the source location. Since the F10.7 index starts high and diverges according to the inverse of the square of the distance, the F10.7 index attenuates quickly and results in one region of extremely high activity at $0°$ latitude and $0°$ longitude, with the rest of the globe exhibiting normal activity.

As another comparison, the electron densities at the same locations as in Figures 15, 16, and 17 were plotted for all the runs using NeQuick, shown in Figure 23. The profile for an F10.7 index of 200 sfu was very similar to that for the diverging F10.7 index computed from the EUVAC model, which is reasonable considering that the background value for the EUVAC model run was 179.6 sfu.

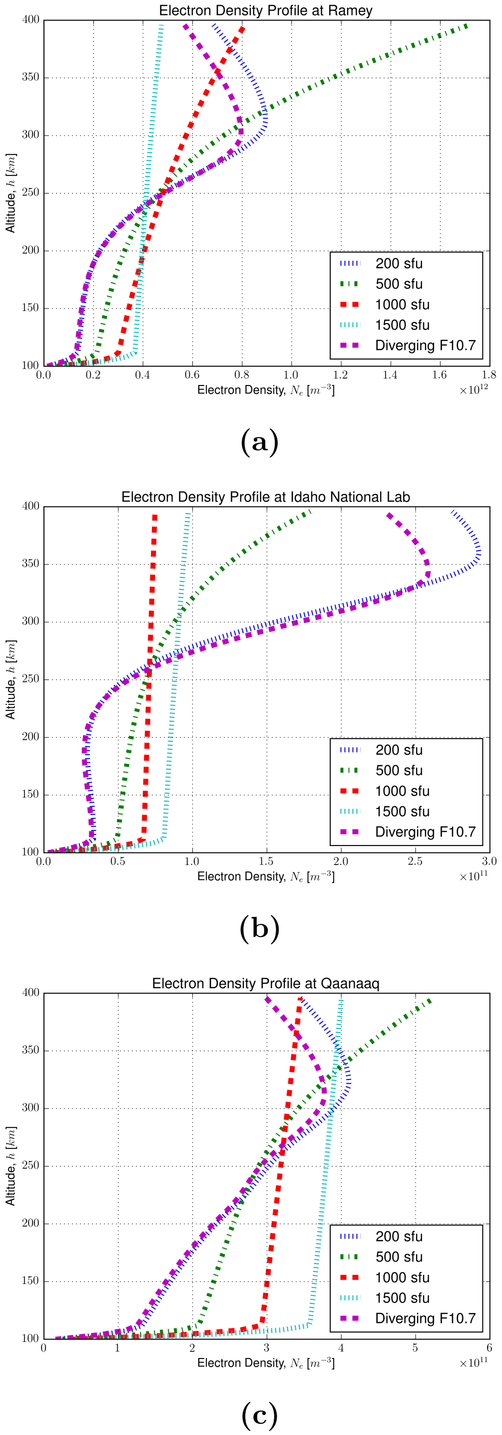

Figure 23. The electron density profiles for the NeQuick runs, for the same locations as the model comparison electron density profiles in Figure 16. Figure 23a is at the Ramey station, Figure 23b is at Idaho National Laboratory, and Figure 23c is at Qaanaaq.

For easy comparison, the results for the TEC of each NeQuick run were recalculated so the TEC values from the background, where the F10.7 index was 179.6 sfu, were subtracted to yield a differential TEC. The differential TECs presented in Figure 24 show the change around the globe due to the modification of the model.

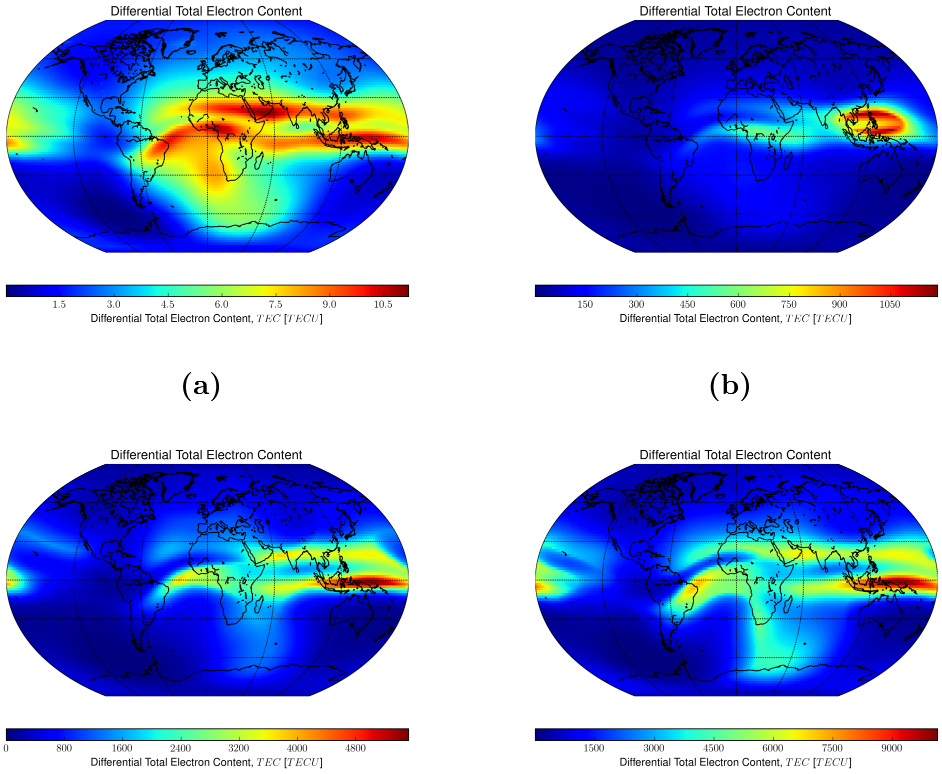

(a) **(b)**

(c) **(d)**

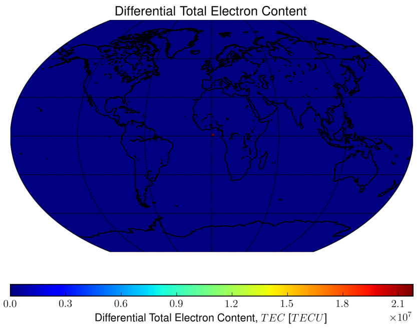

(e)

Figure 24. These are the global maps of the differential TEC for the NeQuick model simulations, run with an F10.7 index of 200 sfu (Fig. 24a), 500 sfu (Fig. 24b), 1,000 sfu (Fig. 24c), 1,500 sfu (Fig. 24d), and with the EUVAC model with an array of indices (Fig. 24e). It is important to note that the scales on each subplot are different due to the extreme variations.

4.2.2 Modified TIE-GCM.

The same studies were then conducted using TIE-GCM, starting with using 200 sfu for the F10.7 index, as illustrated in Figure 25. The results are very similar to the results from NeQuick, though the peaks of hmF2, nmF2, and the TEC values are shifted more to the east. Further, the results are close to those for the maximum parameters as shown in Figure 16.

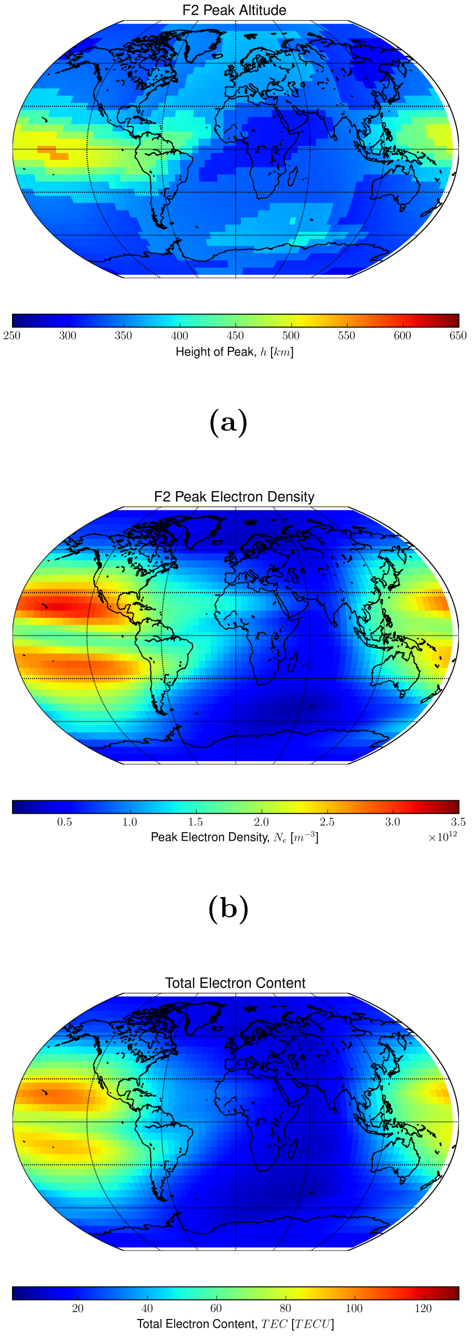

(a)

(b)

(c)

Figure 25. The hmF2 (25a), nmF2 (25b), and TEC (25c) maps for a global F10.7 index of 200 sfu in TIE-GCM. This is considered the baseline test for TIE-GCM in this study and the results are similar to those from the model comparison with the maximum parameters for TIE-GCM.

When the F10.7 index was increased to 500 sfu, the shape of the contours of the maps in Figures 26a, 26b, and 26c were almost identical to those for an F10.7 index of 200 sfu (Fig. 25a, 25b, and 25c). However, the heights of the F_2-region peaks have increased for the higher F10.7 and the total TEC is greater in the highest contours.

It is expected that, even given the increased F10.7 index, that the ionosphere modeled by TIE-GCM would not change as drastically as the ionosphere did with NeQuick. TIE-GCM incorporates more complicated interactions and has a limited response to the F10.7 index.

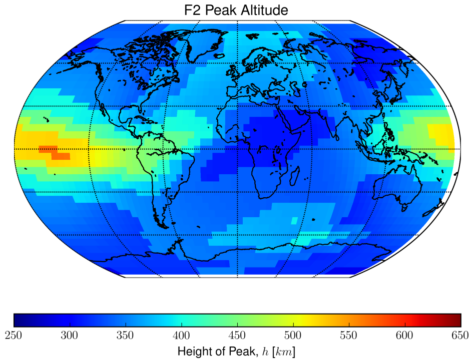

(a)

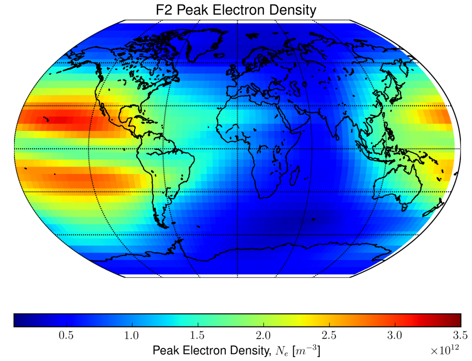

(b)

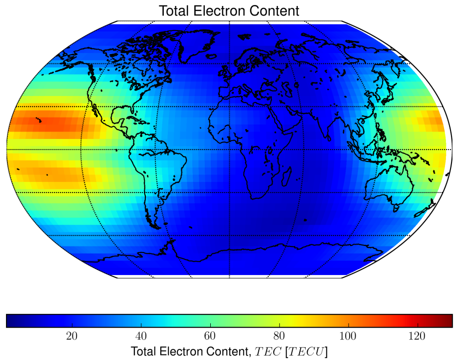

(c)

Figure 26. The hmF2 (26a), nmF2 (26b), and TEC (26c) maps for a global F10.7 index of 500 sfu in TIE-GCM. These results are very similar to those for the F10.7 of 200 sfu, though the peak of the F_2-region and the TEC values are slightly higher, as shown on the scale.

A change of the F10.7 index to 1,000 sfu shows another subtle shift to higher values in the hmF2 map (Fig. 27a) and the TEC map (Fig. 27c), but the nmF2 map (Fig. 27b) remains largely unaffected. This is an expected result, since, again, the model has measures that correct for higher solar activity to keep the ionosphere realistic.

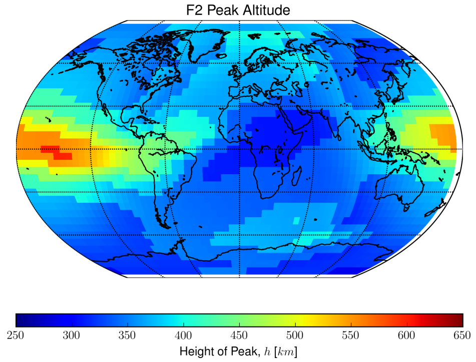

(a)

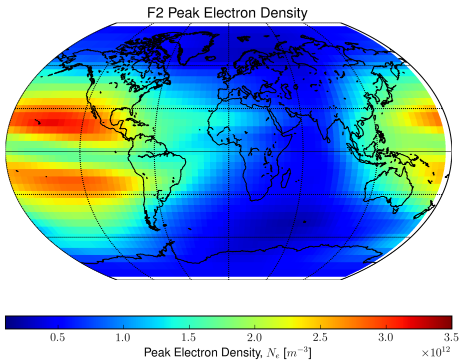

(b)

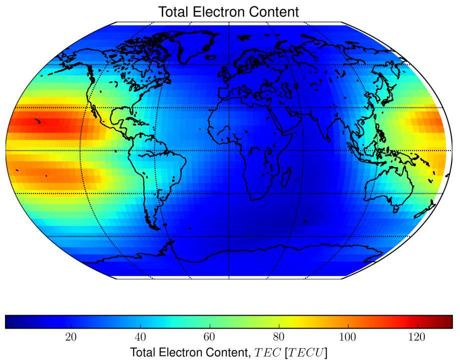

(c)

Figure 27. The hmF2 (Fig. 27a), nmF2 (Fig. 27b), and TEC (Fig. 27c) maps for a global F10.7 index of 1,000 sfu in TIE-GCM. The highest values of hmF2 and TEC are now significantly greater than for an F10.7 index of 200 sfu, but the lowest values remain the same. Thus, the nmF2 appears identical to that of the lower F10.7 index.

The F10.7 index was finally increased to 1,500 sfu. As seen with all other variations, the electron density at the peak of the F_2-region peak, illustrated by the nmF2 map in Figure 28b, did not vary, but the height of the F_2-region peak in the hmF2 map in Figure 28a and the TEC map in Figure 28c are noticeably different, especially when compared to the baselines plots for an F10.7 index of 200 sfu. With the baseline, the highest F_2-region peak was approximately 530 km, whereas with the 1,500 sfu F10.7 index, the peak was approximately 630 km. Further, the highest TEC value at 200 sfu was 102.9630 TECU, while at 1,500 sfu it was 124.2052 TECU. The trend indicates that the increasing F10.7 index only serves to raise the height of the ionosphere, which in turn increases the TEC values as more ionosphere is added to the integral.

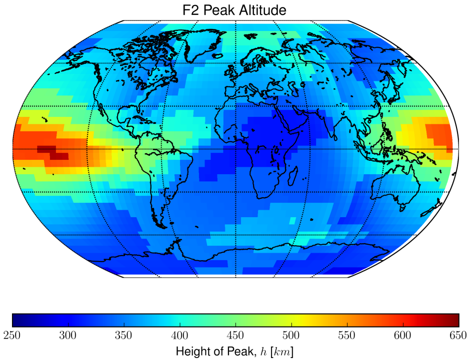

(a)

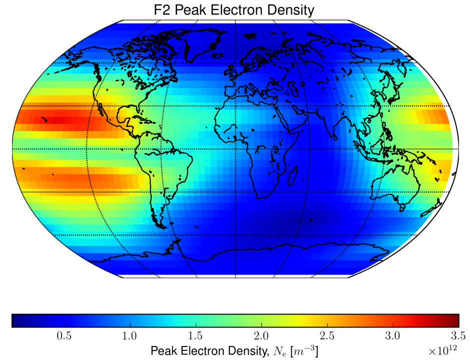

(b)

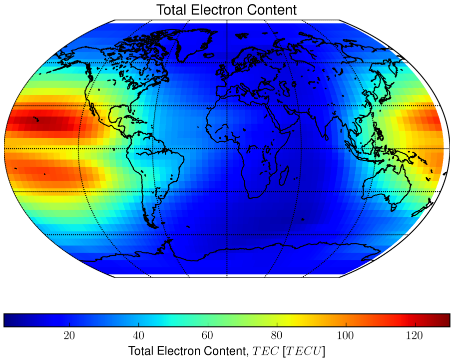

(c)

Figure 28. The hmF2 (28a), nmF2 (28b), and TEC (28c) maps for a global F10.7 index of 1,500 sfu in TIE-GCM. The results of the highest value of the F10.7 index indicate that, while the nmF2 map might remain the same, the hmF2 and TEC maps have risen from the lowest F10.7 index, though not as drastically as NeQuick demonstrated.

The next step was to modify the files in TIE-GCM to incorporate an array of F10.7 indices based on geographic coordinates so that the model can have localized phenomena. This included modifying the chemistry module and the electron/ion temperature module to include an array of F10.7 indices that diverged with the inverse of the distance squared. The F10.7 index at the source, again at 0° latitude and 0° longitude, was calculated with the same method as with NeQuick by reversing the calculations for the EUVAC model. However, much like with the EUVAC model, the results in Figure 29 show that there is no change compared to the baseline results in Figure 25 with an F10.7 index of 200 sfu. This is again due to the divergence of the F10.7 index back to the background value of 179.6 sfu within a short distance of the source.

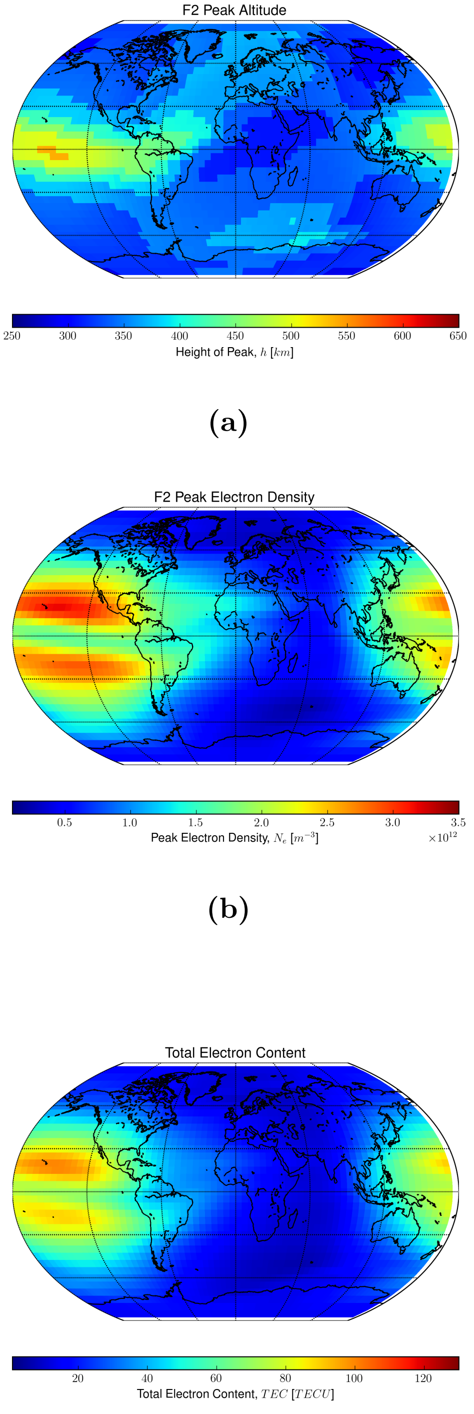

(a)

(b)

(c)

Figure 29. The hmF2 (29a), nmF2 (29b), and TEC (29c) maps for an array of F10.7 indices based on the EUVAC model. The temperature was not modified for these plots. As can be seen, much like the NeQuick results, there is almost no change between these results and the baseline results for TIE-GCM.

Since TIE-GCM is more complicated than NeQuick and has a variety of variables it uses to calculate the electron densities, the model was investigated further and it was found that the calculations for electron density also rely on the temperature. From the calculations for the EUVAC model, it was determined using Wertz and Larson (2007) that a reasonable temperature for the fireball and thus the ionosphere at the source is 10^6 K. This temperature was then added to the background temperature that the model calculates and attenuated by the inverse square of the distance, like the F10.7 index. Since many modules incorporate temperature, all but two of the relevant modules were changed to include the fireball temperature, the exceptions being the cooling by Newton's Law module (newton.F) and the magnetic pressure module (magpres_g.F). The cooling module was not modified since it calculates the cooling rates based on the inputted temperatures, which have already been modified, and the magnetic pressure module was not modified since its arrays cannot handle high temperatures without encountering a memory error. A complete list of modified modules and their respective functions can be found in Table 6.

The modified TIE-GCM was then run, with Figure 30 displaying the results. These results look highly similar to those in the baseline figure, Figure 25. This does not, however, take into account that the energy near the detonation would not dissipate as rapidly due to the thin atmosphere and fewer particle collisions compared to what would happen near the surface.

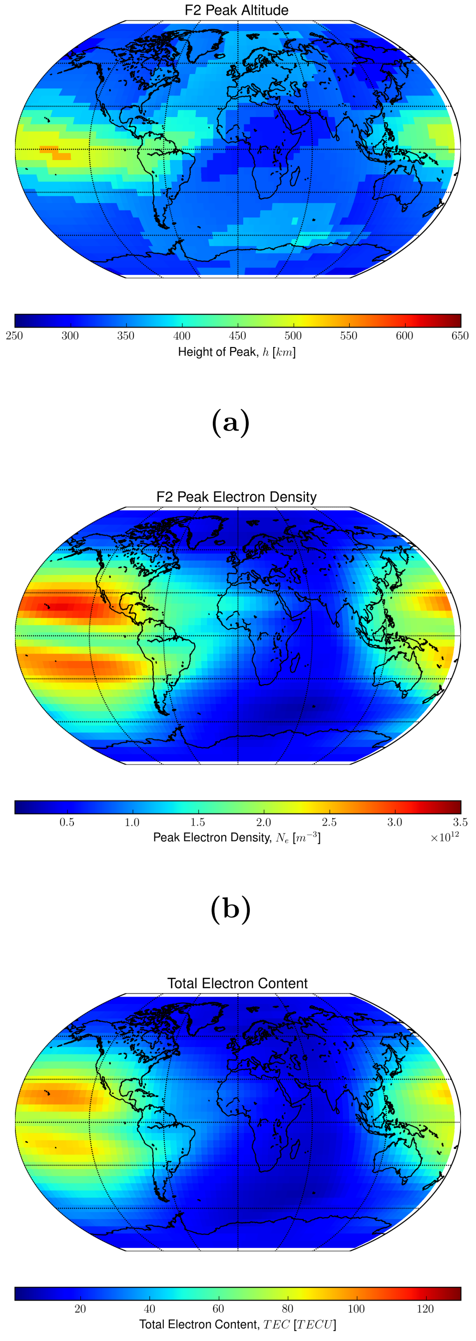

(a)

(b)

(c)

Figure 30. The hmF2 (30a), nmF2 (30b), and TEC (30c) maps for an array of F10.7 indices based on the EUVAC model and an array of temperatures that diverge from the source location according to the inverse square law. Again, these results look very similar to the results for the baseline for TIE-GCM.

To account for the spread of the energy of the fireball in the thinner atmosphere, the temperature was attenuated by 99% for an area with a radius of 100 km from the detonation point before diverging according to the inverse square law. This is a first order approximation and does not accurately reflect the physics in this region, but given that TIE-GCM does not include the chemistry for Compton scattering or the thermodynamic mechanisms to account for the spread of energy from one superheated region, it serves as a crude approximation of the effects.

The results of the approximation, given in Figure 31, do show a noticeable difference in contours, especially concerning the F_2-region peak altitudes shown in Figure 31a and the TEC values in Figure 31c. The heights on the daytime have risen, while the nighttime heights have fallen. The TEC values have also risen where solar activity is highest. The electron density profiles in Figure 32 reflect this, as they have a lower height of the F_2-region peak than for the baseline model. Notably, the map of nmF2 in Figure 31b has not changed.

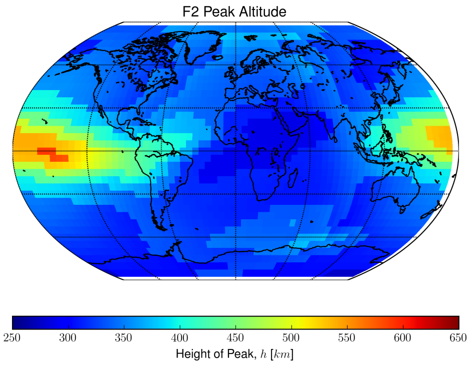

(a)

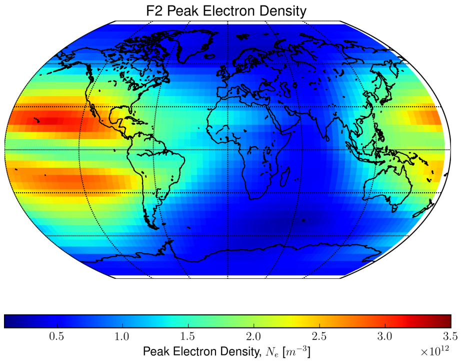

(b)

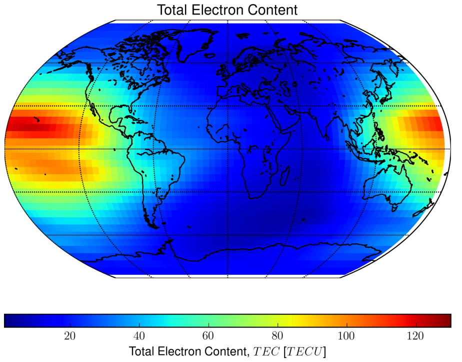

(c)

Figure 31. The hmF2 (31a), nmF2 (31b), and TEC (31c) maps for an array of F10.7 indices based on the EUVAC model and an array of temperatures that are fractionally reduced up to 100 km from the source and then diverge according to the inverse square law. These results show an increase in the altitude of the F_2 peaks, similar to the results of an increased F10.7 index alone.

The combined electron density profiles for the runs of TIE-GCM are displayed in Figure 32, split into the same locations as the previous electron density profiles. The results are almost indistinguishable at low altitudes, but diverge around 200 km for each location. Changing the global F10.7 index from 200 sfu to 1,500 sfu did not vary the electron density until the F_2 peaks around 300 km. The run with the F10.7 index diverging from the detonation location and the run with the F10.7 index and temperature diverging from the detonation location are the same, while the run with the temperature kept constant in the region around the detonation (denoted ”Spread T”) had the greatest variation from the other results. The F_2 peaks of these results are lower than those for the other runs.

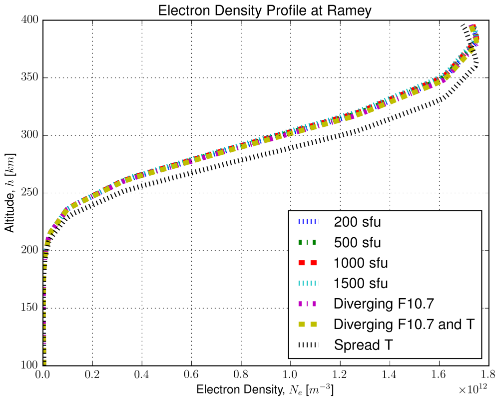

(a)

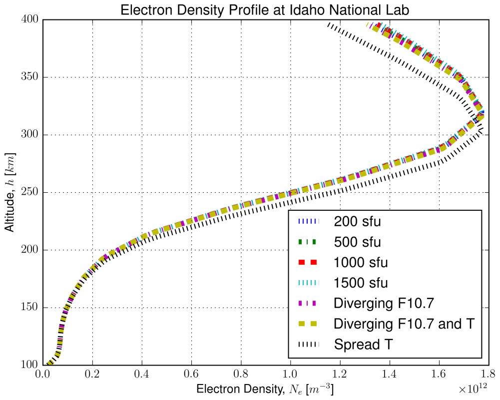

(b)

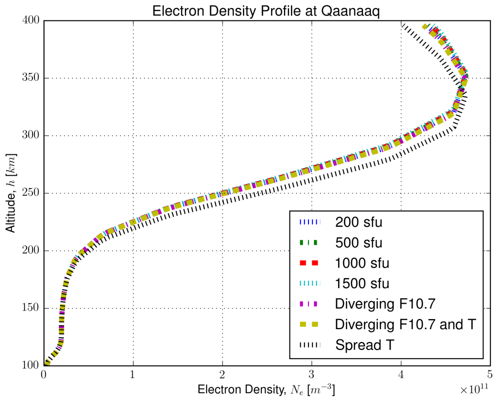

(c)

Figure 32. The electron density profiles for the TIE-GCM runs are plotted together for comparison. Figure 32a is at the Ramey station to represent the equatorial latitudes, Figure 32b is at Idaho National Laboratory for the mid-latitudes, and Figure 32c is at Qaanaaq to illustrate the polar latitudes.

For convenience, the maps of the differential TEC for all the studies in TIE-GCM are provided in Figure 33. The differential TEC values are the TEC values for the chosen day with an F10.7 index of 179.6 sfu subtracted from the values from the model run, showing the change due to the variations.

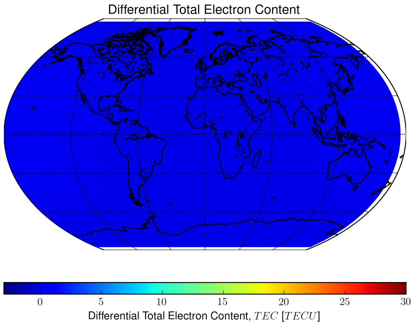
Differential Total Electron Content
0
5
10
15
20
25
30
Differential Total Electron Content, TEC $[TECU]$

(a)

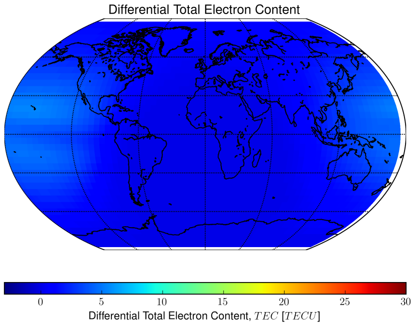
Differential Total Electron Content
0
5
10
15
20
25
30
Differential Total Electron Content, TEC $[TECU]$

(b)

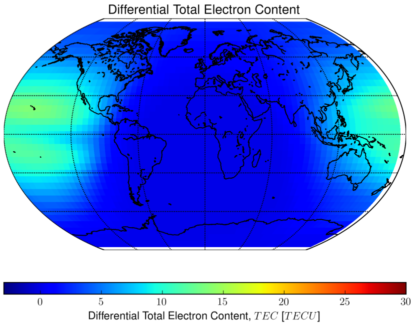
Differential Total Electron Content
0
5
10
15
20
25
30
Differential Total Electron Content, TEC $[TECU]$

(c)

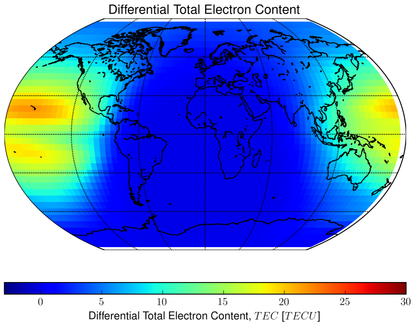
Differential Total Electron Content
0
5
10
15
20
25
30
Differential Total Electron Content, TEC $[TECU]$

(d)

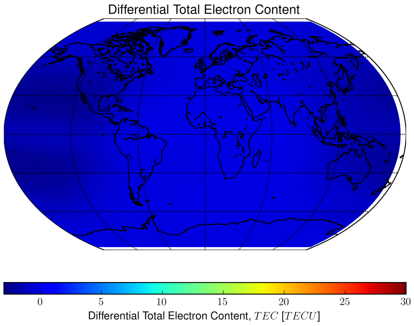
Differential Total Electron Content
0
5
10
15
20
25
30
Differential Total Electron Content, TEC $[TECU]$

(e)

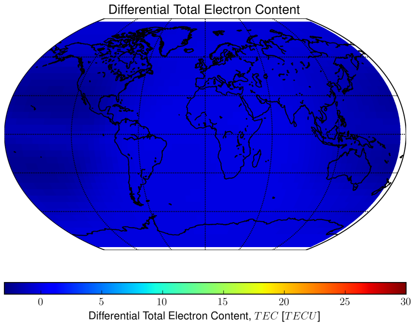
Differential Total Electron Content
0
5
10
15
20
25
30
Differential Total Electron Content, TEC $[TECU]$

(f)

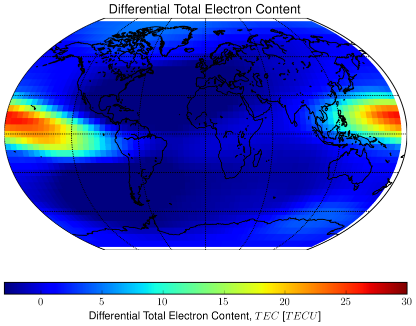

(g)

Figure 33. These are the global maps of the differential TEC for the TIE-GCM simulations, run with an F10.7 index of 200 sfu (Fig. 33a), 500 sfu (Fig. 33b), 1,000 sfu (Fig. 33c), and 1,500 sfu (Fig. 33d); with an array of F10.7 indices (Fig. 33e); the array with the temperature attenuating by the inverse square law (Fig. 33f); and the array with the temperature being first reduced and then being attenuated (Fig. 33g).

4.3 Validation of Models

Since there is little to no information on the ionospheric response from the HAND tests conducted in the late 1950s and early 1960s, there is no way to directly compare the results of the study to any actual data. Therefore, it is worth looking at what is available. Several satellites, including Explorer IV, Injun I, and Telstar-1, were equipped with sensors to measure particle fluxes and were in orbit during many of the tests. The collected omnidirectional electron fluxes from Telstar-1 after Starfish Prime is given in Figure 34, but the fluxes here were taken at altitudes exceeding 1,000 km and were taken in units of [counts/s]. This is included to show the distribution of the electrons around the globe.

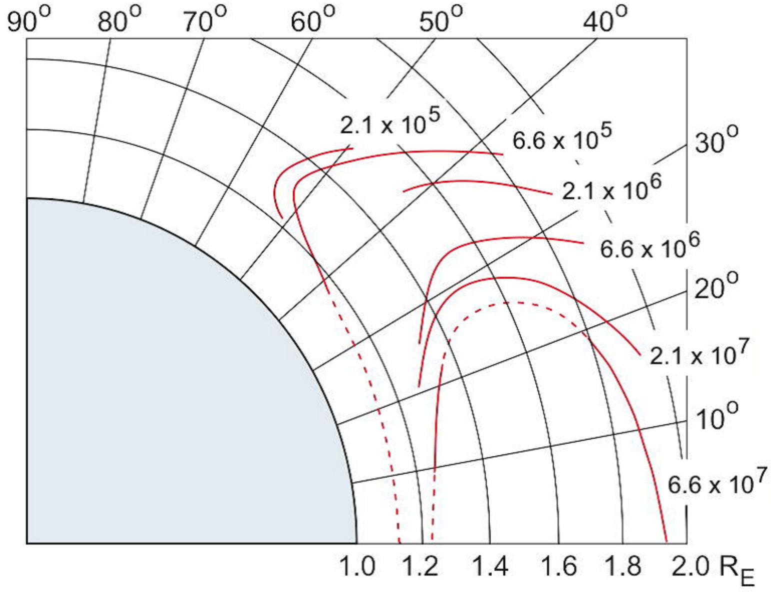

Figure 34. These are the contours of the omnidirectional counting rates, measured in [counts/s], on the electron channel on Telstar-1, presented by Gombosi et al. (2017). The coordinate system is based on the McIlwain's coordinate system using Earth radii and angle from the equator. The data was taken between 11 July 1962 and 15 July 1962.

To give a better understanding of the enhancement in terms of electron fluxes, the time evolution of the omnidirectional counting rates taken by Telstar-1 are shown in Figure 35 for comparison. Since these are fluxes, they are still not directly comparable to the results of the study, but the fluxes can be divided by the velocity of the electrons to get an estimate of the density. Regardless, the data given for these enhanced belts gives an upper limit of what to expect from a HAND.

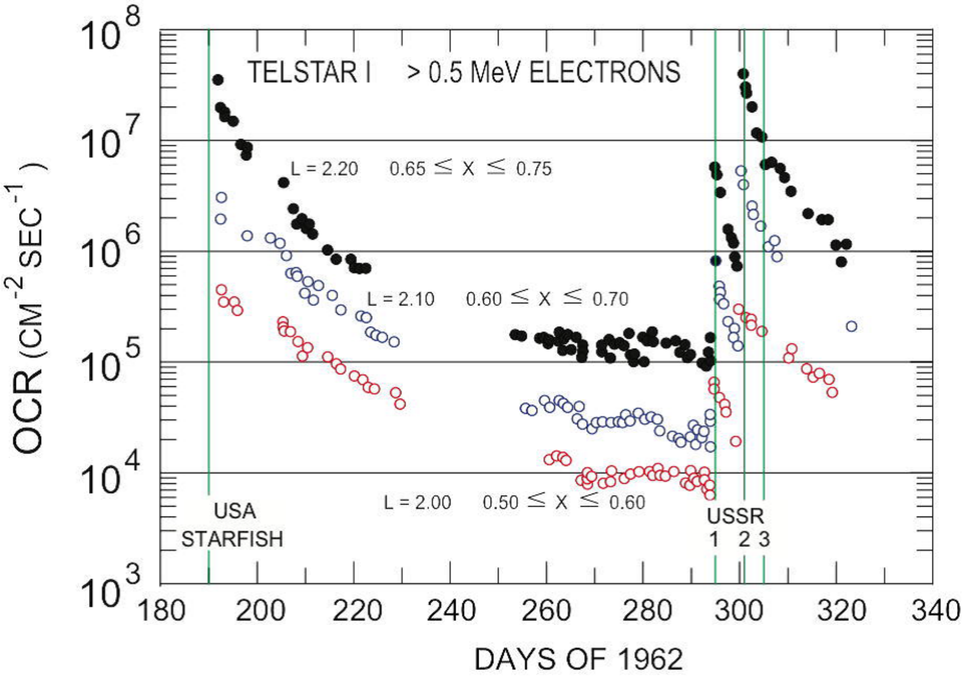

Figure 35. These are the omnidirectional counting rates (OCR) of the electrons taken aboard Telstar-1 taken just after Starfish Prime and extending to after the K PROJECT Tests #184, 187, and 195. Here, L is the McIlwain coordinate and $x = \sqrt{1 - B_0/B}$. Figure from Gombosi et al. (2017).

To calculate an estimate of the speed of an electron at these altitudes, a rough first-order approximation that does not include the initial velocity from the expansion of the diamagnetic cavity for the average equatorial drift velocity is given as

$$< v_d > \approx \frac{6EL^2}{q_e B_{eq} R_E}(0.35 + 0.15 \sin \alpha_{eq}), \tag{28}$$

where E is the energy of the particle, B_{eq} is the equatorial magnetic field strength of 3.11×10^{-5} T and α_{eq} is the pitch angle at the equator. Assuming an α_{eq} of 45° and using the lowest energy of 0.5 MeV for the electrons and the lowest L-value of 2.00 from Figure 35, the velocity is estimated to be 2.7×10^5 m/s. This results in an approximate electron density directly after the detonation of 1.8×10^5 m^{-3}. However, according to Gombosi et al. (2017), the peak flux exceeded 10^9 cm^{-2}s^{-1}, which corresponds approximately to a density of over 4×10^7 m^{-3}. When comparing to the results from NeQuick in Figure 36, where the altitude for the electron density profiles was raised to 25,000 km, it becomes apparent that either the approximate velocity is incorrect or that NeQuick's propagation of the electron densities into the magnetosphere and beyond is flawed. The upper boundary would be more applicable if the ionosphere models extended into the magnetosphere and into the radiation belts.

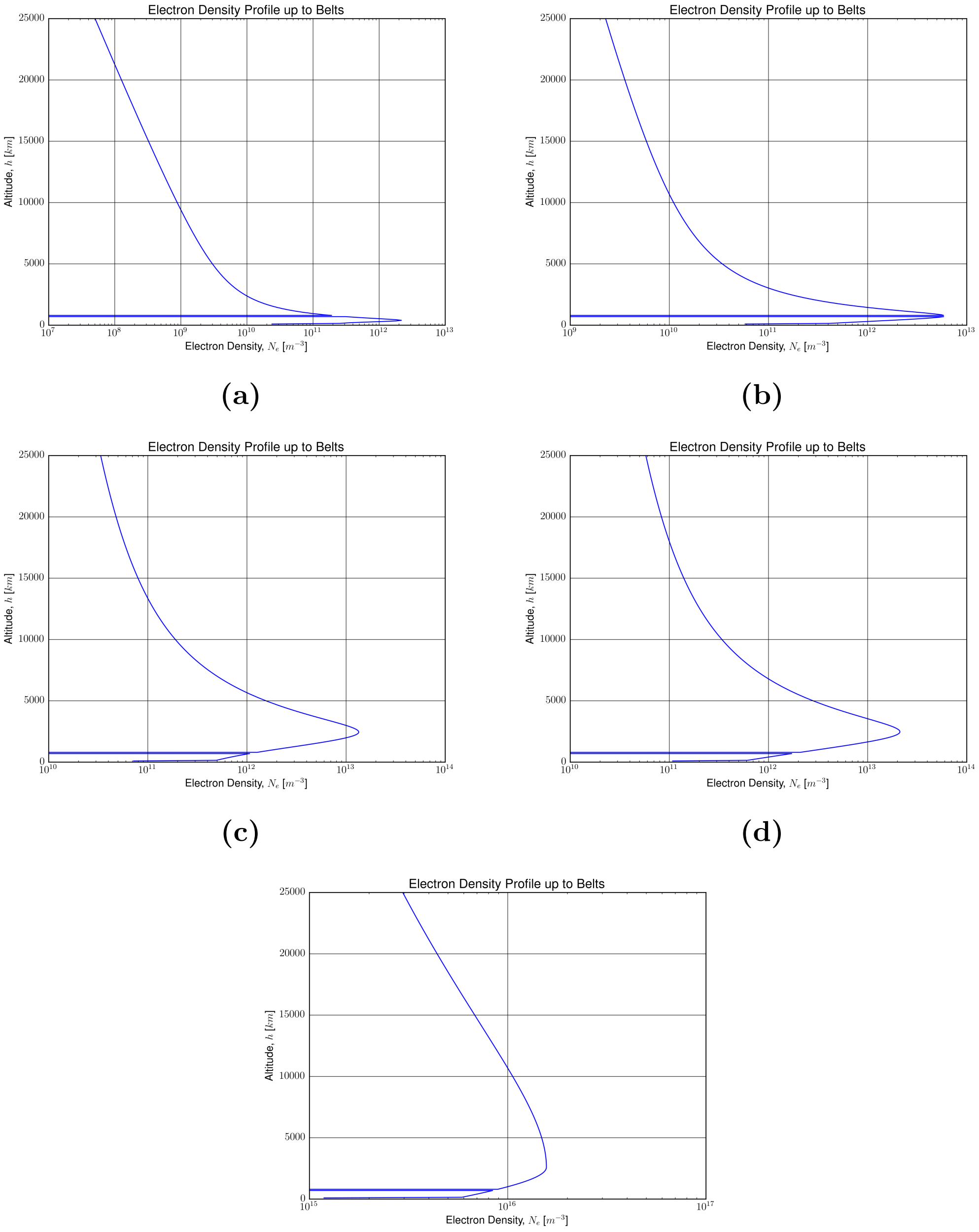

(a)

(b)

(c)

(d)

(e)

Figure 36. These are the electron density profiles at the point of detonation using the NeQuick that extend into the Van Allen radiation belts, run with an F10.7 index of 200 sfu (Fig. 36a), 500 sfu (Fig. 36b), 1,000 sfu (Fig. 36c), 1,500 sfu (Fig. 36d), and with the EUVAC model with an array of indices (Fig. 36e).

However, an easier way to check if the results are realistic is to compare the findings of the study to those of studies that examine solar flare events or geomagnetic storms. One such study by Yue et al. (2016) examined the geomagnetic storm on 17 March 2013. Using a reanalysis algorithm that incorporated approximately 10 satellites and about 450 ground receivers to recalculate the electron densities, the Global Navigation Satellite System (GNSS) data, and TIE-GCM with both the Heelis and Weimer potentials, the paper computed the TEC values for both quiet and storming conditions, displayed in Figure 37 as a differential TEC between reference quiet days and the storm days.

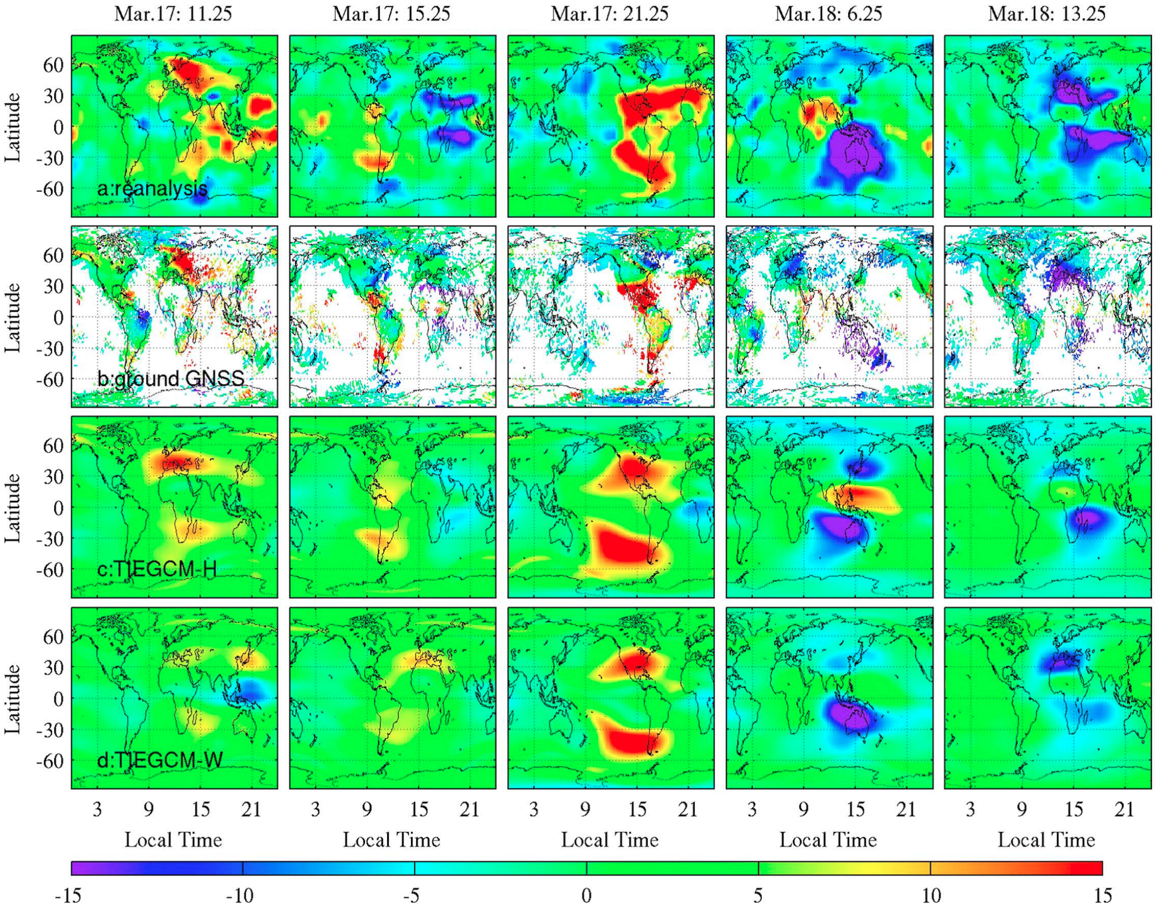

Figure 37. These figures, produced in Yue et al. (2016), show the differential TEC between reference quiet days and the storming days from different sources and models. Figure 37a is from the reanalysis, Figure 37b is from the ground-based GNSS data from the MIT Madrigal database, Figure 37c is the TIE-GCM results using the Heelis potentials, and Figure 37d is the TIE-GCM results using the Weimer potential.

From these plots, it is determined that the maximum difference between TEC for a geomagnetic storm and a baseline ionosphere is 15 TECU in regions of the highest activity. Comparing to the results for TIE-GCM, illustrated in Figure 33, the maximum difference between the modified model and the baseline was also about 25 TECU, so the modifications are larger than the changes demonstrated by this event.

V. Conclusions

5.1 Summary

The results of the initial model comparison revealed that the physics-based ionospheric models could not be varied through the run-on-request feature enough to show an enhancement from an extreme localized event. While SAMI3 was the most responsive to changes in the F10.7 index, SAMI3 does not extend into the polar latitudes due to the way the model is calculated. USU-GAIM did not have options to vary the F10.7 index on the CCMC interface. TIE-GCM had the smallest response from the variation of the F10.7 index but had other attributes that led to its selection to be modified.

The modification of NeQuick to show the response to extreme values of F10.7 resulted in values that were not physical, but illustrated the limitations of the quick-run model. The atmosphere has several restoring methods which would prevent the height of the ionosphere from extending to the F_2-region peak values exhibited in Figure 21a. This study illustrates many of the problems associated with current ionospheric models, especially concerning the chemistry and the reliance on empirical relations. Since NeQuick is an empirically-based climatological model, it is expected that it would not be able to illustrate the complexities of the ionosphere.

When modifying TIE-GCM, it became apparent that the model is heavily reliant on the magnetic parameters and on the temperature rather than the F10.7 index. In fact, though the model documentation states that it uses the EUVAC model to create an EUV spectrum, it does not use the spectrum it calculates. Instead, it uses the F10.7 index to calculate the coefficients for the chemical reactions using an empirical relation and to calculate the ion and electron temperatures, again using empirical formulas. The rest of the model is more influenced by the temperature of the ionosphere, which is why the temperature was modified directly to reflect the temperature change in the atmosphere. The most influential factor, however, were those for the magnetic field, including the power and polar cap potential. The increased temperature in a region, despite only being 100 km in radius, provided a significant change to the hmF2 and TEC values, and indicates that expanding the thermodynamic interactions included in TIE-GCM might prove valuable to modeling the response of the ionosphere to an event such as a HAND.

Lastly, the results were compared to existing data to test the validity of the changes. The only data readily available from Starfish Prime and the other HAND tests are electron fluxes in the Van Allen radiation belts. To compare the flux to the electron density, the velocity of the electrons was approximated, though the first-order approximation of the density from the flux did not match the densities propagated to the radiation belts by NeQuick. Thus, the data from Starfish Prime is not compatible for comparison to the ionospheric models. However, it was possible to compare the results of this study to the data from geomagnetic storms, which, using the test case of the 17 March 2013 storm, proved to be in good agreement in terms of the maximum differential TEC values.

In conclusion, despite the promising comparison between the geomagnetic storm and the results, it was determined that the current ionospheric models are not sufficient to model a HAND. The first reason for this is that the models rely too heavily on proxy variables that are time-averaged; for example, the F10.7 index is a daily value and is not supposed to represent the fluctuations in solar activity, only an average. The models are also, despite being physics-based, reliant on numerous empirical relations. This makes the addition of physics for Compton scattering or the addition of an EMP to the calculated electric and magnetic fields difficult if not impossible without rewriting the respective modules completely. Then, the models do not have the resolution to see localized events such as a HAND; TIE-GCM had one of the smallest resolutions of 2.5° in latitude and longitude, but this is not sufficient to see the variations caused by a nuclear detonation. If the current ionspheric models were to be used for the express purpose of modeling the response to a HAND, the models would need an extensive rework of the chemistry and electric fields, which was beyond the scope of this study.

5.2 Recommendations for Future Work

The first item to be addressed is finding a better method of propagating the temperature from a localized phenomena that can super-heat, or super-cool, a region of the ionosphere. This can be done using the density as an indicator of when to begin using Newton's law of cooling, or proper thermodynamics can be added into the model to account for this. The method examined in this study only approximated the effects that would be seen.

Given that TIE-GCM is primarily driven by currents and the magnetic field, TIE-GCM was not the ideal model to use for modification. However, SAMI3 is heavily influenced by solar activity, as it is a chemistry-focused model. This model could be modified in a similar way to TIE-GCM to use an array of F10.7 indices to use with its chemical equations, and the results could be compared to those found in this work.

If research were to continue to use the existing ionospheric models to attempt to describe extreme phenomena such as a HAND, it would first be necessary to adjust the chemistry to allow for Compton interactions. It would also be necessary to include chemistry for the *D*-region to be able to model the lower atmosphere, where these interactions would typically take place. This could then be expanded to include the resulting EMP phases that occur due to the chemical and electromagnetic interactions in the ionosphere, specifically in the lower ionosphere.

However, due to the numerous limitations of the ionospheric models, it is recommended to use the models developed for a HAND and instead add in an ionosphere that incorporates all the chemistry of the ionosphere, including the chemistry that applies to HANDs. This code would then more accurately reflect the propagation of the EMP and the formation of the source region. This would allow for further investigation into how a HAND would propagate in various ionospheric conditions, including high and low solar activity and geomagnetic storming. It would also allow for the addition of a radiation belt model to incorporate the enhancement of the inner belt.

It is the conclusion of this study that the current ionospheric models are insufficient for extreme event modeling, especially when considering anthropogenic effects. Due to the numerous empirical calculations, such as for the chemical reaction coefficients, and reliance on parameters that are not reflective of the environment like the F10.7 index, it is recommended that the parameters and calculations be replaced. There are multiple papers on alternatives or improvements to the F10.7 index (Acebal, 2008; Schunk and Nagy, 2009) and multiple sensors, such as those on the GOES satellites, that measure the EUV flux without the need for a proxy that recalculates the same fluxes using something like the EUVAC model. The empirical calculations that use the proxy parameters are also subject to the same flaws as the parameters, such as being limited to quiet activity. The calculations should be reinvestigated and the reaction coefficients rederived to be based on first principles. These should then be incorporated into a new, full-physics model for the ionosphere. This model should be able to more accurately reflect the state of the ionosphere and may prove to be better at both nowcasting and forecasting than current models. Having a model with equations derived from first principles would also allow for additional physics such as radio occultation and phenomena such as sporadic-E to be included.

Appendix A

A.1 EUVAC Model Bins

The EUVAC model relies on the modified reference flux F74113 and a scaling factor A, which are binned according to wavelength. The values were reported in **?** and are reproduced here in Table **??** for reference.

Table 5. These are the parameters for the EUVAC model. The F74113 fluxes in bins 1 and 2 were tripled, and bins 3 and 4 were doubled, according to ?.

Bin, i	Wavelength, λ [nm]	F74113 [$\times 10^{-9}$ photons cm^{-2} s^{-1}]	A
1	5-10	1.200	1.0017×10^{-2}
2	10-15	0.450	7.1250×10^{-3}
3	15-20	4.800	1.3375×10^{-2}
4	20-25	3.100	1.9450×10^{-2}
5	25.632	0.460	2.7750×10^{-3}
6	28.415	0.210	1.3768×10^{-1}
7	25-30	1.679	2.6467×10^{-2}
8	30.331	0.800	2.500×10^{-2}
9	30.378	6.900	3.3333×10^{-3}
10	30-35	0.965	2.2450×10^{-2}
11	36.807	0.650	6.5917×10^{-3}
12	35-40	0.314	3.6542×10^{-2}
13	40-45	0.383	7.4083×10^{-3}
14	46.522	0.290	7.4917×10^{-3}
15	45-50	0.285	2.0225×10^{-2}
16	50-55	0.452	8.7583×10^{-3}
17	55.437	0.720	3.2667×10^{-3}
18	58.433	1.270	5.1583×10^{-3}
19	55-60	0.357	3.6583×10^{-3}
20	60.976	0.530	1.6175×10^{-2}
21	62.973	1.590	3.3250×10^{-3}
22	60-65	0.342	1.1800×10^{-2}
23	65-70	0.230	4.2667×10^{-3}
24	70.336	0.360	3.0417×10^{-3}
25	70-75	0.141	4.7500×10^{-3}
26	76.515	0.170	3.8500×10^{-3}
27	77.041	0.260	1.2808×10^{-2}
28	78.936	0.702	3.2750×10^{-3}
29	75-80	0.758	4.7667×10^{-3}
30	80-85	1.625	4.8167×10^{-3}
31	85-90	3.537	5.6750×10^{-3}
32	90-95	3.000	4.9833×10^{-3}
33	97.702	4.400	3.9417×10^{-3}
34	95-100	1.475	4.4167×10^{-3}
35	102.572	3.500	5.1833×10^{-3}
36	103.191	2.100	5.2833×10^{-3}
37	100-105	2.467	4.3750×10^{-3}

A.2 Modified TIE-GCM Files

This provides a list of the files in TIE-GCM that were modified, what the file or module's purpose was, and which variables were modified.

Table 6. These are the source code files of TIE-GCM that were modified, including their purpose and which variables were modified. The input.F and hist.F files were not included since these must be changed to incorporate the changes in the input file. The variable f107 corresponds to the F10.7 index, tn is the neutral temperature, ti is the ion temperature, and te is the electron temperature.

File	Purpose	Variable Modified
chapman.F	Compute line integrals based on the Chapman model	tn
chemrates.F	Calculate chemical reaction rates	f107, tn, te, ti
comp.F	Advances O and O_2 as species	tn
comp_o2o.F	Calculates the array for sources and sinks	tn
cpktkm.F	Defines the diagnostics of CP, KT, and KM	tn
elden.F	Calculate electron density	tn
lamdas.F	Determine the ion drag coefficients	tn, te, ti
minor.F	Compute minor species composition	tn
oplus.F	Propagate O^+ as a species	tn, te, ti
qjion.F	Ion chemistry contribution to the neutral gas heating and O_2 dissociation	tn
qjnno.F	Neutral gas heating and O_2 dissociation from N and NO chemistry	tn
qjoule.F	Ion Joule heating	tn
settei.F	Calculate electron and ion temperatures	f107, tn, te, ti

A.3 Example TIE-GCM Input File

An example of the input files used for the TIE-GCM simulations is provided in Figure 38. This is a modified file to account for the added module that calculates the HAND F10.7 index array and the temperature attenuation. This also details which source files and other parameters were used for the simulations. The details of the parameters can be found in the TIE-GCM documentation.

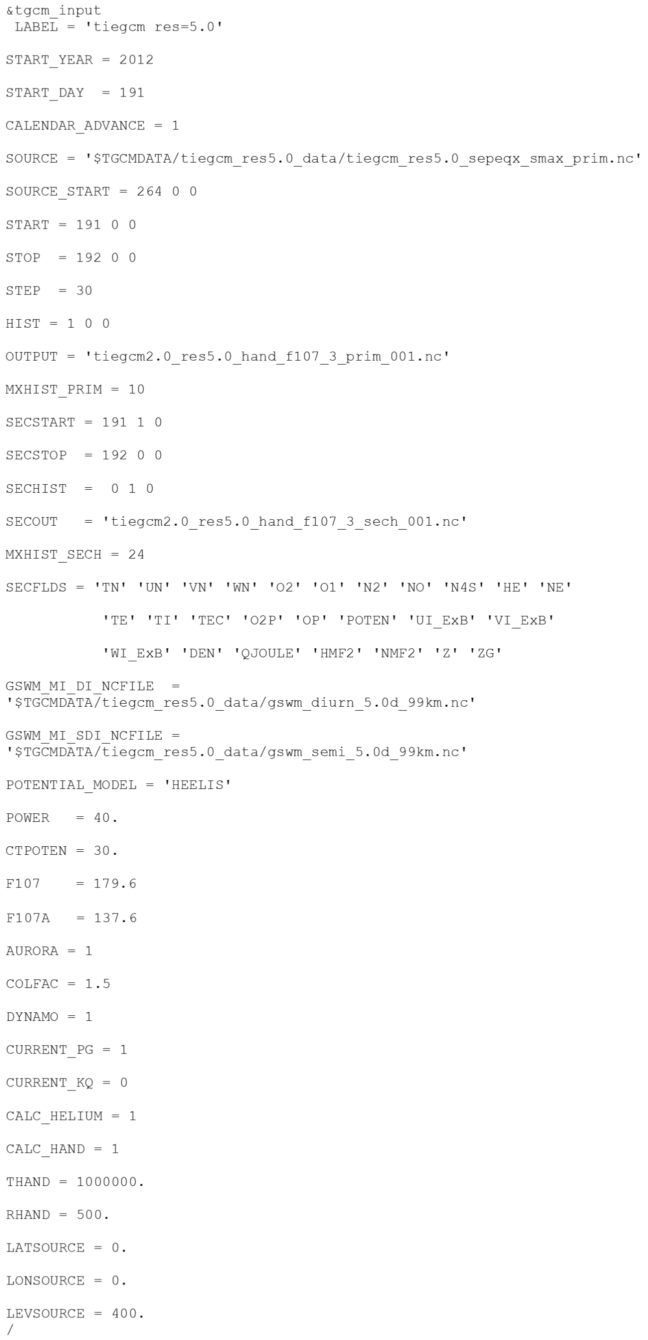

```
&tgcm_input
 LABEL = 'tiegcm res=5.0'

START_YEAR = 2012

START_DAY  = 191

CALENDAR_ADVANCE = 1

SOURCE = '$TGCMDATA/tiegcm_res5.0_data/tiegcm_res5.0_sepeqx_smax_prim.nc'

SOURCE_START = 264 0 0

START = 191 0 0

STOP   = 192 0 0

STEP   = 30

HIST = 1 0 0

OUTPUT = 'tiegcm2.0_res5.0_hand_f107_3_prim_001.nc'

MXHIST_PRIM = 10

SECSTART = 191 1 0

SECSTOP  = 192 0 0

SECHIST  =  0 1 0

SECOUT   = 'tiegcm2.0_res5.0_hand_f107_3_sech_001.nc'

MXHIST_SECH = 24

SECFLDS = 'TN' 'UN' 'VN' 'WN' 'O2' 'O1' 'N2' 'NO' 'N4S' 'HE' 'NE'

           'TE' 'TI' 'TEC' 'O2P' 'OP' 'POTEN' 'UI_ExB' 'VI_ExB'

           'WI_ExB' 'DEN' 'QJOULE' 'HMF2' 'NMF2' 'Z' 'ZG'

GSWM_MI_DI_NCFILE  =
'$TGCMDATA/tiegcm_res5.0_data/gswm_diurn_5.0d_99km.nc'

GSWM_MI_SDI_NCFILE =
'$TGCMDATA/tiegcm_res5.0_data/gswm_semi_5.0d_99km.nc'

POTENTIAL_MODEL = 'HEELIS'

POWER   = 40.

CTPOTEN = 30.

F107    = 179.6

F107A   = 137.6

AURORA = 1

COLFAC = 1.5

DYNAMO = 1

CURRENT_PG = 1

CURRENT_KQ = 0

CALC_HELIUM = 1

CALC_HAND = 1

THAND = 1000000.

RHAND = 500.

LATSOURCE = 0.

LONSOURCE = 0.

LEVSOURCE = 400.
/
```

Figure 38. This is an image of the .inp file that was used for the TIE-GCM simulations. The CALC_HAND parameter was a 0/1 selection to chose whether to calculate the effects of a detonation, while THAND was the temperature of the fireball in [K], RHAND was the radius of the fireball in [m], LATSOURCE and LONSOURCE were the geographic coordinates of the detonation, and LEVSOURCE was the altitude of the detonation. All other parameters are the same for a normal TIE-GCM file using the Heelis potential model.

Bibliography

Acebal, A. O. *Extending F10 .7's Time Resolution to Capture Solar Flare Phenomena.* PhD thesis, Utah State University, 2008.

Baker, D. N., Kanekal, S. G., Hoxie, V. C., Henderson, M. G., Li, X., Spence, H. E., Elkington, S. R., Friedel, R. H. W., Goldstein, J., Hudson, M. K., Reeves, G. D., Thorne, R. M., Kletzing, C. A., and Claudepierre, S. G. A Long-Lived Relativistic Electron Storage Ring Embedded in Earth's Outer Van Allen Belt. *Science*, 340 (6129):186–190, 4 2013. ISSN 0036-8075. doi: 10.1126/science.1233518.

Bridgman, C. J. *Introduction to the Physics of Nuclear Weapons Effects.* Defense Threat Reduction Agency, Ft. Belvoir, first edition, 2001.

Chapman, S. The absorption and dissociative or ionizing effect of monochromatic radiation in an atmosphere on a rotating earth. *Proceedings of the Physical Society*, 43(1):26–45, 1931. ISSN 09595309. doi: 10.1088/0959-5309/43/1/305.

Codrescu, M. The influence of the ionosphere on GPS Operations. In *Applications of GPS/GNSS in NOAA*, Boulder, CO, 2007. Space Weather Prediction Center, NCEP/NWS/NOAA. URL `ftp://ftp.ngdc.noaa.gov/STP/GPS_GNSS/Mihail’s.pdf`.

Conrad, E. E., Gurtman, G. A., Kweder, G., Mandell, M. J., and White, W. W. Collateral Damage to Satellites from an EMP Attack. Technical report, Defense Threat Reduction Agency, Ft. Belvoir, 2010.

Defense Threat Reduction Agency. Burst Height Impacts EMP Coverage. *The Dispatch*, 5(3):8, 2016. URL `http://www.dtra.mil/Portals/61/Documents/DTRIAC/DispatchJune2016.pdf`.

Dupont, D. G. Nuclear Explosions in Orbit. *Scientific American*, pages 100–107, 6 2004.

European Commission. Ionospheric Correction Algorithm for Galileo Single Frequency Users. 2016.

Foster, B. TIEGCM Documentation. Technical report, NCAR High Altitude Observatory, 2016.

Foster, J. S. J., Gjelde, E., Graham, W. R., Hermann, R. J., Kluepfel, H. M., Lawson, R. L., Soper, G. K., Wood, L. L. J., and Woodard, J. B. Report of the Commission to Assess the Threat to the United States from Electromagnetic Pulse (EMP) Attack : Critical National Infrastructures. Technical report, Commission to Assess the Threat to the United States from Electromagnetic Pulse (EMP) Attack, 2008.

Gombosi, T. I., Baker, D. N., Balogh, A., Erickson, P. J., Huba, J. D., and Lanzerotti, L. J. Anthropogenic Space Weather. *Space Science Reviews*, 212(3-4):985–1039, 2017. ISSN 15729672. doi: 10.1007/s11214-017-0357-5.

Gurnett, D. A. and Bhattacharjee, A. *Introduction to Plasma Physics*. Cambridge University Press, New York, second edition, 2017. ISBN 978-1-107-02737-4.

Huba, J. D., Maute, A., and Crowley, G. SAMI3_ICON: Model of the Ionosphere/-Plasmasphere System. *Space Science Reviews*, 212(1-2):731–742, 10 2017. ISSN 0038-6308. doi: 10.1007/s11214-017-0415-z.

Hutchinson, I. H. *Introduction to Plasma Physics*. Massachusetts Institute of Technology, 2001. URL `http://silas.psfc.mit.edu/introplasma/index.html`.

Krane, K. S. *Introductory Nuclear Physics*. John Wiley & Sons, Hoboken, first edition, 1988. ISBN 978-0-471-80553-3.

Longmire, C. L. On the Electromagnetic Pulse Produced Nuclear Explosions. *IEEE Transactions on Antennas and Propagation*, AP-26(1):3–13, 1978.

Morrow, D. P. *Motion of the debris from a high-altitude nuclear explosion : simulations including collisionless shock and charge exchange*. PhD thesis, Naval Postgraduate School, 2014.

Nava, B., Coïsson, P., and Radicella, S. M. A new version of the NeQuick ionosphere electron density model. *Journal of Atmospheric and Solar-Terrestrial Physics*, 70 (15):1856–1862, 2008. ISSN 13646826. doi: 10.1016/j.jastp.2008.01.015.

Pisacane, V. L. *The Space Environment and Its Effects on Space Systems*. AIAA Press, Reston, second edition, 2016. ISBN 978-1-62410-353-7.

Popik, T. S., Kearns, J. T., Baker, G. H., Cooper, H. F., and Harris, W. R. High Consequence Scenarios for North Korean Atmospheric Nuclear Tests with Policy Recommendations for the U. S. Government High Consequence Scenarios for North Korean Atmospheric Nuclear Tests with Policy Recommendations for the U. S. Government. 2017.

Qian, L., Burns, A. G., Emery, B. A., Foster, B., Lu, G., Maute, A., Richmond, A. D., Roble, R. G., Solomon, S. G., and Wang, W. The NCAR TIE-GCM: A Community Model of the Coupled Thermosphere/Ionosphere System. In Huba, J. D., Schunk, R. W., and Khazanov, G., editors, *Modeling the Ionosphere Thermosphere System*, pages 72–83. American Geophysical Union, Boulder, CO, 2013. ISBN 9780875904917. doi: 10.1029/2012GM001297.

Regi, M. ULF power fluctuations in the solar-wind parameters and their relationship with the relativistic electron flux at the geosynchronous orbit. *Il Nuovo Cimento*, 39(C):285–295, 2016. doi: 10.1393/ncc/i2016-16285-x.

Reinisch, B. W. and Galkin, I. A. Global Ionospheric Radio Observatory (GIRO). *Earth, Planets and Space*, 63(4):377–381, 4 2011. ISSN 1343-8832. doi: 10.5047/eps.2011.03.001.

Richards, P. G., Fennelly, J. A., and Torr, D. G. EUVAC: A solar EUV Flux Model for aeronomic calculations. *J. Geophys. Res*, 1994. ISSN 0148-0227. doi: 10.1029/94JA00518.

Ridley, A. J., Deng, Y., and Tóth, G. The global ionosphere-thermosphere model. *Journal of Atmospheric and Solar-Terrestrial Physics*, 68(8):839–864, 2006. ISSN 13646826. doi: 10.1016/j.jastp.2006.01.008.

Russel, C. T., Luhmann, J. G., and Strangeway, R. J. *Space Physics: An Introduction*. Cambridge University Press, Cambridge, first edition, 2016. ISBN 978-1-107-09882-4.

Scherliess, L., Schunk, R. W., Gardner, L. C., Zhu, L., Eccles, J. V., and Sojka, J. J. The USU-GAIM Data Assimilation Models for Ionospheric Specifications and Forecasts. 2017.

Schunk, R. and Nagy, A. *Ionospheres: Physics, Plasma Physics, and Chemistry*. Cambridge University Press, New York, second edition, 2009. ISBN 978-0-521-87706-0.

Stuckenberg, D., Woolsey, R. J., and DeMaio, D. Electromagnetic Defense Task Force 2018 Report. Technical report, Air University LeMay Center for Doctrine Development and Education, Maxwell Air Force Base, AL, 2018.

U.S. Department of Energy. United States Nuclear Tests: July 1945 through September 1992. *DOE/NV–209-Rev 16*, (July 1945), 2015.

Wahl, A. C. Nuclear-Charge Distribution and Delayed-Neutron Yields for Thermal-Neutron-Induced Fission of U-235, U-233, and Pu-239 and for Spontaneous Fission of Cf-252. *Atomic Data and Nuclear Data Tables*, 39(1):1–156, 1988. ISSN 0031899X.

Wertz, J. R. and Larson, W. J. *Space Mission Analysis and Design.* Microcosm Press and Springer, Hawthorne, CA and New York, NY, third edition, 2007. ISBN 978-1881883-10-4.

Yue, X., Wang, W., Lei, J., Burns, A., Zhang, Y., Wan, W., Liu, L., Hu, L., Zhao, B., and Schreiner, W. S. Long-lasting negative ionospheric storm effects in low and middle latitudes during the recovery phase of the 17 March 2013 geomagnetic storm. *Journal of Geophysical Research: Space Physics*, 121(9):9234–9249, 9 2016. ISSN 21699380. doi: 10.1002/2016JA022984.

Zhu, L., Schunk, R. W., Jee, G., Scherliess, L., Sojka, J. J., and Thompson, D. C. Validation study of the Ionosphere Forecast Model using the TOPEX total electron content measurements. *Radio Science*, 41(05):6, 2006. doi: 10.1029/2005RS003336.

REPORT DOCUMENTATION PAGE

Form Approved
OMB No. 0704–0188

1. REPORT DATE *(DD–MM–YYYY)* 23–03–2019	**2. REPORT TYPE** Master’s Thesis	**3. DATES COVERED** *(From — To)* Oct 2017 — Mar 2019

4. TITLE AND SUBTITLE

Modeling High-Altitude Nuclear Detonations
Using Existing Ionospheric Models

5a. CONTRACT NUMBER

5b. GRANT NUMBER

5c. PROGRAM ELEMENT NUMBER

6. AUTHOR(S)

Schwalbe, Sophia Gloria, 2d Lt, USAF

5d. PROJECT NUMBER

5e. TASK NUMBER

5f. WORK UNIT NUMBER

7. PERFORMING ORGANIZATION NAME(S) AND ADDRESS(ES)

Air Force Institute of Technology
Graduate School of Engineering and Management (AFIT/EN)
2950 Hobson Way
WPAFB OH 45433-7765

8. PERFORMING ORGANIZATION REPORT NUMBER

AFIT-ENP-MS-19-M-092

9. SPONSORING / MONITORING AGENCY NAME(S) AND ADDRESS(ES)

Defense Advanced Research Projects Agency
Defense Sciences Office
675 North Randolph Street
Arlington, VA 22203
COMM (703) 526-2801
Email: Charlton.Lewis@darpa.mil

10. SPONSOR/MONITOR’S ACRONYM(S)

DARPA/DSO

11. SPONSOR/MONITOR’S REPORT NUMBER(S)

12. DISTRIBUTION / AVAILABILITY STATEMENT

DISTRIBUTION STATEMENT A: APPROVED FOR PUBLIC RELEASE; DISTRIBUTION UNLIMITED

13. SUPPLEMENTARY NOTES

This material is declared a work of the U.S. Government and is not subject to copyright protection in the United States.

14. ABSTRACT

One threat to the United States is a nuclear weapon being detonated at high altitude over the country. The resulting electromagnetic pulse (EMP) could devastate the nation. Despite its destructive nature, the response of the ionosphere to such an event is poorly understood. This study assesses if existing ionospheric models, which are used to nowcast and forecast ionospheric changes, can be used to model the response to a high-altitude nuclear detonation (HAND). After comparing five ionosphere models, the Thermosphere-Ionosphere-Electrodynamics General Circulation Model (TIE-GCM) was selected and modified to incorporate an array of F10.7 indices to serve as a proxy for the localized heightened extreme ultraviolet activity and, using the temperature of the fireball attenuated over distance, drive the chemistry. It was found that the modified model had an increase in electron content over the standard model that was in good agreement with the changes resulting from a geomagnetic storm. However, the examined ionospheric models are not sufficient to simulate the effects of a HAND due to the limitations in the models’ calculations.

15. SUBJECT TERMS

High-Altitude Nuclear Detonations, HANE, EMP, Ionosphere, Ionospheric Models

16. SECURITY CLASSIFICATION OF:			**17. LIMITATION OF ABSTRACT**	**18. NUMBER OF PAGES**	**19a. NAME OF RESPONSIBLE PERSON**
a. REPORT	**b. ABSTRACT**	**c. THIS PAGE**			Dr. Robert Loper, AFIT/ENP
U	U	U	UU	114	**19b. TELEPHONE NUMBER** *(include area code)* (937) 255-3636, x4333; Robert.Loper@afit.edu

Standard Form 298 (Rev. 8–98)
Prescribed by ANSI Std. Z39.18